LRP 449/92 Februar 1992

X- AND O-MODE ECH BREAKDOWN AND STARTUP IN TCA

D.R. Whaley, T.P. Goodman, A. Pochelon,
R. Behn, A. Cardinali, B.P. Duval, B. Joye,
M.Q. Tran

submitted for publication to Nuclear Fusion

X- and O-Mode ECH Breakdown and Startup in TCA

D. R. Whaley, T. P. Goodman, A. Pochelon, R. Behn,
A. Cardinali†, B. P. Duval, B. Joye, M. Q. Tran

Centre de Recherches en Physique des Plasmas,
Association Euratom-Confédération Suisse,
Ecole Polytechnique Fédérale de Lausanne, 21 Av. des Bains,
CH-1007 Lausanne, Switzerland

We have performed a comparative study of X- and O-mode high field side launch for ECH breakdown and startup of tokamak plasmas. We observe that X-mode power is not absorbed at the cyclotron resonance but uniquely at the upper hybrid resonance, displaced to the low field side of the cyclotron resonance. O-mode power, however, is absorbed at the cyclotron resonance as well. We also observe that the displacement of the upper hybrid resonance to the low field side with O-mode launch is significantly smaller than with X-mode launch due to the lower densities produced at the same microwave power level. The result is a more central and less localized breakdown with O-mode launch. The breakdown characteristics of X- and O-mode launch are seen to affect the position of the initial plasma current centroid in the poloidal cross section. We observe a strong correlation between the initial current ramp rate and the initial plasma current position which is most likely due to the dependence of the plasma inductance, toroidal electric field, and field-line connection lengths on the plasma major radius. O-mode launch starts the plasma more centrally than X-mode launch and results in higher current ramp rates. X-mode startup occurs further to the low field side where current ramp rates are observed to be poor.

† Permanent address: Associazione EURATOM-ENEA sulla Fusione, I-00044 Frascati, Italy

I. Introduction

High-power microwave injection has proven to be an effective method to improve the startup performance of tokamaks. This electron cyclotron heating (ECH) startup assist has been shown to significantly decrease the loop voltage required for startup while increasing the reliability and reproducibility of startup plasmas. The range of fill pressures and stray magnetic fields over which startup is achievable is extended over that of ohmic startup. Delay of the current rise after loop voltage turn-on is decreased with ECH assist and current ramp rates are increased over those of pure ohmic startup at equivalent loop voltages. These general characteristics have been seen on several machines [1-6].

The ECH power may be launched into the plasma region of a tokamak from the high field side (HFS) or low field side (LFS) with X-, O-, or mixed-mode polarization. The choice of the type of launch which will yield the most efficient startup over the widest range of operating parameters is important for future devices. Many early tokamak ECH-assisted startup results come from experiments with the ECH power launched in either the TE_{01} or TE_{02} mode. The injected beam was thus of mixed polarization and the specific effects of X- or O-mode breakdown could not be separated. Other startup experiments have used TE_{11} launch which creates a somewhat linearly-polarized beam but still contains a significant amount of cross polarization. Several experiments also launch the HE_{11} mode, a TE_{11}-TM_{11} hybrid mode [7], producing a beam with small cross polarization. With HE_{11} launch, well-defined X- or O-mode plasma excitation is possible.

Although most present experiments control the polarization of the launched ECH power, few results have been published on the comparative effectiveness of the possible launching schemes. Very early, X- and O-mode were launched on WT-I [2] vertically from the top of the tokamak and no difference in the startup

characteristics of the two modes was seen. This occurred presumably because with top vertical launch, X- and O-mode are both poorly absorbed on the first pass and mode mixing occurred when the power was reflected from the vacuum vessel walls opposite the launching waveguide. X- and O-mode ECH assist was also used on CLEO [8] and generally poorer performance was seen with X-mode launch than with O-mode launch. The ECH power, however, was launched from the LFS and the result was most likely dominated by reflection of the X-mode power from the R-cutoff located just in front of the launching waveguide. The aim of our experiments, therefore, is to determine the differences between X- and O-mode breakdown in tokamak plasmas and how these differences affect tokamak startup. Since an X-mode beam is cutoff from the LFS, we launch an HE_{11} beam from the HFS with the X- or O-mode polarization easily changeable between shots.

We present the paper as follows. The experimental configuration is described in Sec. II. This includes a description of TCA, the ECH system and several of the more important diagnostics. We discuss the general X- and O-mode breakdown features in Sec. III. This includes a discussion of absorption at the electron cyclotron resonance layer and the upper hybrid (UH) resonance layer. Sec. IV discusses the effects of the breakdown characteristics of X- and O-mode launch on TCA startup with some remarks on the general operation of TCA. Conclusions are summarized in Sec. V.

II. Experimental Configuration

TCA is an air-core circular cross-section tokamak [9] with a major radius of $R=0.615m$ and a minor radius of $a=0.18m$. The toroidal magnetic field is limited to values at or below $B_\phi = 1.6T$. TCA has a non-continuous vacuum vessel, separated electrically at two toroidal locations. The vacuum vessel is boronized regularly [10].

The ECH system [11] is shown in Fig. 1. The *39GHz* cylindrical cavity gyrotron, designed and constructed by CRPP and ABB, outputs a TE_{02} beam with a maximum measured efficiency of *42%*. The gyrotron was tested to *250kW* pulsing into a matched, octanol-filled microwave load. For the startup experiments reported here, however, the ECH power seldom exceeded *125kW* ($0.32MW/m^3$ of plasma; $0.13MW/m^3$ of vessel volume). A wave-number spectrometer, located above the gyrotron, measures the TE_{02} mode purity to be *98%*. The microwave beam is then converted ($TE_{02} \rightarrow TE_{01} \rightarrow TE_{11} \rightarrow HE_{11}$) to the HE_{11} mode as it passes through the *11m* of microwave line to the tokamak. The calculated line conversion efficiency is 90% [11]. The cross polarization of the beam at tokamak injection is measured to be $<1.5\%$, the measurement limit. The quartz vacuum window is located inside the TCA vacuum vessel at the end of the microwave waveguide to prevent vacuum breakdown in the line at the cyclotron resonance. The entire line is continually flushed with CO_2 at atmospheric pressure to prevent line arcing. Arc detectors are located at both the gyrotron window and the TCA quartz vacuum window.

The TCA poloidal cross section and launch geometry are shown in Fig. 2. The microwave power, launched through the vacuum quartz window, is reflected into the plasma region from a stainless-steel ellipsoidal microwave mirror. The mirror focuses the beam, reducing the e^{-2} (power) beam divergence from $13.4°$ to $8.5°$ halfwidth with an e^{-2} beam diameter of *7cm* on the tokamak axis. The mirror is steerable with the accessible regions of the poloidal cross section shown between the cross-hatched lines in Fig. 2. Toroidal launching angles between $\pm 25°$ to the radial are also possible, though since the toroidal angle was found to have little influence on breakdown or startup for either X- or O-mode (see discussion in Sec. III), all data presented here, unless explicitly stated, is for injection directly along the radial. Shields have been placed on either side of the mirror to reduce deposits on the mirror and quartz window. The cyclotron resonance can be placed between $x \equiv r/a = -0.5$ (quartz window) and $x = +0.5$ (maximum field). Receiving horns (2 open-ended Q-band waveguides) placed opposite the mirror in the same poloidal

plane measure microwave transmission for both X- and O-mode polarizations. The O-mode transmission measurements are useful for estimating first-pass absorption efficiency in the low-density startup plasmas where refraction effects are not significant. For X-mode launch, however, the UH resonance and R-cutoff lying just in front of the X-mode receiving horn result in a complete loss of the X-mode transmitted signal once even the lowest density plasma has been created.

Since plasma absorption of X- and O-mode microwave radiation are markedly different, we use several diagnostics to determine the spatial absorption characteristics of X- and O-mode launch. Line-integrated H_α emission is recorded, with high spatial resolution, by a 100-channel H_α camera, resolving horizontal (along the major radius) power deposition profiles. An optical spectrometer recording plasma emission in the wavelength range from 7250Å to 7800Å complements the H_α camera. This line-integrated emission measured along eight chords produces vertical power deposition profiles with reasonable spatial resolution. The data presented in this paper for the H_α camera and the optical spectrometer are shown in uninverted form. A five-channel microwave interferometer also measures horizontal electron density profiles. These profile diagnostics all have good temporal resolution with acquisition rates varying from *1.5kHz* to *10kHz*. The geometry of these diagnostics is shown in Fig. 3.

III. Breakdown

We perform two sets of experiments to determine the breakdown and startup characteristics of X- and O-mode launch. In the breakdown experiments, microwave power is launched into the TCA vacuum vessel in the absence of an applied loop voltage, V_L. Therefore no large directed plasma current develops. This allows us to determine the general breakdown characteristics of X- and O-mode launch without the effect of plasma current, the rotational transform of which spreads the spatial

absorption profiles. Also with driven current, the H_α line quickly burns through and the profiles becomes hollow, dominated by ionization of neutral influx from the edge. No vertical field is applied for the breakdown experiments. In the startup experiments the ohmic heating transformers are energized at the beginning of the shot, creating the loop voltage necessary to start the plasma once ECH breakdown occurs. The different effects of X- and O-mode breakdown on the startup of the plasma may then be seen. The startup scenario is described in Sec. IV.

A. Breakdown at the Electron Cyclotron and Upper-Hybrid Resonances

The H_α camera (Fig. 3) measures the horizontal H_α emission profile every $650\mu s$. The H_α camera has a high spatial resolution of $4mm$ on the horizontal axis. For the breakdown experiments, microwave power is launched into the vacuum vessel without an applied loop voltage, and the resulting H_α emission is used to determine the location of the breakdown. We assume a low percentage ionization until burnthrough is seen and use the emission peaks as indications of peak absorption. An example of the contours of the H_α emission for O-mode launch is shown in Fig. 4. The contours show two distinct breakdown regions. The position of the peak located to the HFS, is constant in time and corresponds to breakdown at the cyclotron resonance. The location of the cyclotron resonance layer is calculated from the magnetic field:

$$x_{\omega_{ce}} = \left(\frac{B_m}{B_{res}} - 1\right)\frac{R}{a} \tag{1}$$

where B_{res} = *resonant magnetic field for 39GHz radiation* and B_m = *measured magnetic field at* $x = 0$, and plotted as curve (A) in Fig. 4. The UH resonance layer occurs where the magnetic field and density satisfy the condition:

$$\omega_o = \omega_{UH} = (\omega_{ce}^2 + \omega_{pe}^2)^{1/2} \qquad (2)$$

We use the five-channel interferometer to measure the horizontal electron density profile. This electron density profile and the R^{-1} magnetic field profile then determine the location where Eq. (2) is satisfied. Since the measured densities are line-averaged vertically (see Fig. 3), we must assume a vertical profile shape to calculate the peak density values (for a given horizontal position) used to determine the shift of the UH resonance layer to the LFS of the cyclotron resonance. Figure 4 shows the calculated UH resonance position each $650\mu s$ for a flat vertical profile (B') and a peaked vertical profile (B'') (with a parabolic peaking factor of 2.5). Densities at the limiter radius are assumed to be zero. We observe that the non-stationary peak located to the LFS of Fig. 4 closely follows the computed UH resonance location throughout the shot. Figure 4 therefore shows well-resolved evidence (spatially and temporally) of breakdown at both the cyclotron resonance and the UH resonance. Note that the absorption near the UH resonance layer is much larger than that near the cyclotron layer. This is seen more clearly in the later example of Fig. 9. The movement of the breakdown location to the UH resonance is clearly observed on all TCA shots with $V_L = 0V$ and we see that after $1\text{-}2ms$, depending on gas fill, wall conditioning, and microwave power, the majority of the absorption is displaced to the LFS of the cyclotron resonance. This has important consequences for tokamak startup.

B. X/O-Mode Breakdown Characteristics

X- and O-mode launch exhibit significantly different breakdown characteristics. Differences are measured in first-pass absorption efficiencies, ionization rates, electron densities per kW of ECH power, heating rates, and breakdown location. The data that we present in this paper are always taken from consecutive TCA discharges with the polarization of the ECH power rotated between X- and O-mode

within the given series. This assures identical tokamak conditions for comparison of the two launched modes.

The transmission detector located opposite the mirror measures X- and O-mode transmitted power. This detector, shown in Fig. 2, consists of two Q-band open-ended waveguides oriented $90°$ to each other. Transmission measurements are shown for both X- and O-mode in Fig. 5 as a function of density. This data was taken over a series of ~ 70 discharges of both breakdown ($V_L=0V$) and startup ($V_L=1\text{-}2V$) discharges to cover the entire density range. The range of densities for breakdown shots is indicated in the figure as $\bar{n}_e < 3x10^{12}cm^{-3}$, for which refraction effects are negligible. For these low breakdown densities, we observe O-mode power to be poorly absorbed on the first pass. As the density increases during started discharges, the transmission decreases to zero indicating, as expected, better absorption at higher densities. Care must be taken at high densities, however, since refraction effects at $39GHz$ start to become important at densities above $n_e \sim 1x10^{13}cm^{-3}$. Although the first-pass O-mode absorption shown in Fig. 5 is relatively poor, it is significantly higher than what we would expect from calculation. This might indicate the existence of a high temperature, low density non-Maxwellian plasma component located at the cyclotron resonance. The poor O-mode first-pass absorption leads to wall reflections and therefore a mixing of modes. It also results in a spatial spreading of the energy deposition across the entire vertical resonance layer, shown below. We see that the transmitted signal for X-mode launch is negligible for all but the zero density case. This is presumably due to the UH resonance and R-cutoff lying in front to the X-mode receiving horn. Evidence, though, of good first-pass X-mode absorption as well as power spreading resulting from poor first-pass O-mode absorption is seen in the vertical plasma emission profiles of X- and O-mode launch, shown in Figs. 6. X-mode launch results in a peaked emission profile, a signature of localized power deposition possible only in the absence of wall reflections. We see, however, that the O-mode launch emission profile is quite uniform vertically although, in the first pass, the beam e^{-2} power level

intercepts only 20% of the resonance layer. We believe that multiple reflections from the vacuum vessel wall are responsible for the spreading of the deposition profile. These profiles of plasma emission characterize X- and O-mode launch and are observed in all discharges. We see in Fig. 6(a) that X-mode power is poorly absorbed on the first pass during the first $\sim 800\mu s$, evidenced by the uniform emission profile at the very beginning of the discharge. We believe that this is the time required to create the initial plasma necessary to absorb the X-mode power. RF pickup on the microwave interferometer precludes measurement of the electron density profiles during the first few milliseconds of the plasma discharge, however. Other evidence of poor O-mode and good X-mode first-pass absorption is presented later in this section where O-mode breakdown characteristics are seen to be mixed with those of X-mode through wall reflections while X-mode launch does not exhibit such mixed-mode breakdown characteristics.

We also observe differences in the total ionization capability of the two modes. X-mode launch generally creates a larger average electron density than O-mode launch. Figure 7 shows the average electron density for a series of discharges with varying B_ϕ. The electron density measured using the five interferometer chords are averaged over the microwave pulse of $20ms$ with $P_{ECH} = 50kW$. The average density created with X-mode launch is seen to be 20%-40% higher than that for O-mode launch over the entire range of magnetic field. The ionization capability of either mode is seen to decrease as the toroidal magnetic field is increased and the cyclotron and UH resonance layers move to the LFS. In general we also observe a higher ionization rate with X-mode launch evidenced by a faster H_α line burnthrough. The higher electron densities and higher ionization rates are characteristic of X-mode launch and are seen in every case.

In this breakdown section we have included data from a series of startup shots showing that heating rates are also measured to be higher with X-mode launch. Figure 8(a) shows the carbon-IV burnthrough time for a series of started ECH-assisted discharges at varying microwave power. Carbon-IV has an ionization

potential of ~$65eV$ and reaches burnthrough with X-mode launch in ~65%-75% of the time required for O-mode launch. Although the electron distributions are not expected to be Maxwellian, the faster burnthrough of the Carbon-IV line does indicate faster general heating rates and higher overall "temperatures."

Bolometry measurements indicate a difference in impurity levels at the beginning of started discharges for X- and O-mode launch, arising from the different breakdown properties of the two modes. The plasma radiated power is measured by a 16 channel bolometer array with $P_{rad}/n_e \sim n_i f_i$ where i is the impurity species and f_i is a non-constant function of T_e. Since we observe that the maximum of P_{rad} always occurs $7\text{-}8ms$ after the beginning of the ECH pulse for both X- and O-mode launch, independent of the ECH power (contrary to the temperature behavior with P_{ECH} of Fig. 8(a)), we can exclude a strong temperature dependence on the radiated power. We therefore assume P_{rad}/n_e to be dominated by the impurity density n_i. Fig. 8(b) shows the peak P_{rad}/n_e during the first $10ms$ of the shots of Fig. 8(a). We see that the radiated power is consistently higher for O-mode launch for the entire range of P_{ECH}. This indicates a higher impurity influx resulting from a higher microwave wall loading already seen inherent to O-mode launch. This effect of higher impurity levels is seen, though, to disappear within $20ms$ of the current startup and does not affect the impurity concentration (radiated power) later in the discharge for startup with either mode.

The H_α camera situated ~$1.5m$ above the midplane of TCA measures the horizontal H_α emission profiles of breakdown plasmas. We use the H_α profiles to determine the breakdown location for both X- and O-mode launch. One example is shown in Fig. 9 for X- and O-mode launch at $P_{ECH} = 80kW$. The prefill pressure is $P_{fill} \sim 3x10^{-5}Torr$ - a typical prefill pressure used for discharges in TCA. Each point shown on the H_α profiles corresponds to one pixel of the H_α camera. The on-axis magnetic field of $1.38T$ places the cyclotron resonance at $x=-0.03$. For O-mode launch the two breakdown peaks discussed in Sec. III A, are clearly seen. The peak

to the HFS, located at the cyclotron resonance, remains at x=-0.03 during the entire microwave shot. The peak to the LFS, located at the UH resonance, moves as the density and profile shape change. The profiles shown in the figure are measured at the very beginning of the microwave pulse. A majority of the O-mode power is seen to be absorbed at the UH resonance but significant absorption still appears at the cyclotron resonance. On the contrary, for X-mode launch, breakdown occurs only near the UH resonance with no significant absorption occurring at the cyclotron resonance. Also, due to its higher ionization rates, X-mode launch creates higher densities which move the UH resonance further to the LFS of the cyclotron resonance than O-mode launch for the same microwave power. This displacement is shown as Δx_{UH} in Fig. 9 and is ~50% larger for X-mode launch. Note also that there is no breakdown for either mode for $x \leq x_{\omega_{ce}}$. Electron density profiles are not available due to rf pickup on the interferometer circuit during the first few *ms* of the microwave pulses. These characteristics of X- and O-mode breakdown are seen for all microwave power levels, prefill pressures, and toroidal magnetic fields. For O-mode launch, the breakdown is, therefore, generally less localized and more central (horizontally) than for X-mode launch, due to absorption at both the cyclotron and UH resonance layers and the fact that the UH resonance layer does not displace as far to the LFS as with X-mode launch. X-mode breakdown is seen to be more localized and displaced further to the LFS. It is also seen to be more localized vertically - as seen on the plasma emission profiles of Fig. 6. The location of the breakdown is seen to be important for tokamak startup efficiency and is discussed in Sec. IV.

The H_α contours of Fig. 4 and the H_α profiles of Fig. 9 indicate that strong absorption occurs near the UH resonance layer. Previous experiments have seen this anomalous absorption occur to the LFS of the cyclotron resonance [3,12,13] near the UH resonance, though to our knowledge no published data exists showing either clear spatial resolution of the cyclotron and UH absorption or well-resolved

temporal evolution of the movement of the UH resonance to the LFS of the cyclotron resonance for breakdown plasmas.

This anomalous absorption at the UH resonance layer can be explained by a linear conversion of the X-mode power to an electron-Bernstein wave. This conversion can be essentially 100% efficient [14]. The power of the electron-Bernstein wave is then absorbed as it propagates back from the conversion region. There is also, however, substantial evidence that the power absorption is a result of parametric decay of the X-mode power into an electron-Bernstein and a lower-hybrid wave at the UH resonance. This has been seen to occur both in low-density, low-temperature plasmas [15,16,17] such as those found at breakdown, and in hot, dense, developed plasmas [18, 19]. The decay has been verified experimentally where waves of both the electron-Bernstein and lower-hybrid wave frequencies (fulfilling the frequency-matching condition) were seen to be generated near the UH resonance. The phenomenon was seen to be a threshold phenomenon indicative of a non-linear process. The power coupled to the lower-hybrid waves accounts for observed anomalous ion heating [16, 18, 19]. In TCA, we also observe this effect. Figure 10 shows ion heating resulting from injection of X-mode power. This is seen with a neutral particle analyzer (NPA) measuring hot charge-exchanged neutrals escaping from the plasma region. This effect greatly diminishes in TCA, as in [18] and [19], as the launch is changed from X- to O-mode.

Figure 9 also shows negligible X-mode absorption at the cyclotron resonance. Anisimov [20] shows that X-mode absorption at the cyclotron resonance becomes negligibly small when the plasma electron density is such that it satisfies the relation:

$$\frac{\omega_{pe}^2}{\omega_o^2} > 0.04 . \qquad (3)$$

In this regime, the electric field vector of the elliptically polarized X-mode wave is changed to rotate in a sense opposite to that of the plasma electrons, and the wave-electron coupling is lost. For $39GHz$, a density of $n_e > 0.8x10^{12}cm^{-3}$ is required to satisfy Eq. (3), a density regime quickly reached in standard TCA discharges. This loss of wave-electron coupling is not expected to occur for O-mode launch. The above relation (Eq. 3) is valid for a toroidal launch angle of $\Theta_T=0°$ where Θ_T is the angle between the beam path and the radial. In TCA, the microwave beam may be launched with a toroidal angle of $-25° < \Theta_T < +25°$. One might expect a large effect of the toroidal launch angle on the X-mode breakdown characteristics, specifically, a significantly improved absorption at the cyclotron resonance with a non-zero toroidal launch angle. We observe, however, that with the low temperature plasmas present at breakdown, the breakdown characteristics are practically independent of the toroidal launch angle. This is best illustrated in the H_α profiles of Fig. 11. The figure shows the H_α profiles for injection both along the radial and with a toroidal launch angle of $\Theta_T=25°$. The profiles are seen to be identical in shape and amplitude with the exception of the region around the cyclotron resonance where slightly higher absorption is seen for the $\Theta_T=25°$ case. Though the difference is small, it is a reproducible effect. The electron density profiles show no measurable change with a change in Θ_T. We have calculated the expected X-mode absorption at the cyclotron resonance as a function of electron temperature and toroidal launch angle for parameters of typical TCA discharges. These calculations were performed using a wave propagation and absorption code for a hot slab plasma in the electron cyclotron range of frequencies [21]. The calculations show that for electron temperatures of a few eV and below, the X-mode absorption at the cyclotron resonance is expected to be very small ($<5\%$) even for toroidal launch angles of up to $\Theta_T=25°$. It should be noted that Thomson scattering measurements, sensitive to temperatures above $30eV$, were never able to measure an electron temperature during breakdown. Only for electron temperatures in excess of a few hundred eV, well above those of TCA

breakdown plasmas, is the absorption at the cyclotron resonance for a launch angle of $\Theta_T = 25°$ calculated to be complete.

O-mode breakdown characteristics, however, show no observable change as Θ_T is varied. This is to be expected as O-mode cyclotron absorption is calculated to be practically independent of injection angle for $0° < \Theta_T < +25°$. Some absorption at the cyclotron resonance may also be a result of wall reflections and mode conversion followed by absorption at very shallow angles of propagation where absorption is calculated to be efficient even for low electron temperatures. In this case, the observed cyclotron resonance width, measured by the H_α camera and calculated to be a function of electron temperature, is consistent with the upper T_e limit given by Thomson scattering measurements. The fact that the measured breakdown characteristics of X- or O-mode launch do not change significantly with changes in Θ_T results in the startup characteristics being independent of Θ_T for startup with either mode.

As a final remark in this section, the fact that breakdown at the UH resonance occurs in TCA for O-mode launch is assumed to be a result of the mode mixing that occurs with wall reflections after the poor O-mode first-pass absorption described earlier in this section. X-mode breakdown, on the contrary, does not exhibit mixed-mode breakdown behavior (i.e. no breakdown at the cyclotron resonance) again indicating that X-mode power is well absorbed on its first pass through the plasma volume.

IV. ECH-Assisted Startup

Microwave power is launched in either X- or O-mode polarization to create the initial plasma required to achieve startup at low applied loop voltage ($0.15V/m < E_\phi < 0.50V/m$). Figure 12 illustrates a typical startup sequence. A flat loop voltage is applied from $t = 0$. As shown in the figure, an unavoidable $4V$ loop

voltage spike occurs at the V_L turn-on time. The microwave pulse is therefore delayed to allow the loop voltage to stabilize to the desired value. During the *20ms* before the microwave turn-on no plasma is created in the TCA vessel as *8-10V* are typically required for pure ohmic startup. The density, H_α emission, and start of the current rise appear simultaneously with the injection of ECH power. For these experiments, the loop voltage is held constant for the duration of the discharge and the current ramp rates for discharges of equal V_L are compared. For all cases, vertical and horizontal field feedback is set for central positioning.

We immediately observe differences in the startup behavior of X- and O-mode launch. An example of startup at $P_{ECH} = 100kW$, $\Delta t_{ECH} = 10ms$, $x_{\omega_{ce}} = 0$ for both X- and O-mode launch is shown in Fig. 13. O-mode launch creates a steady current ramp which continues during and after the shutoff of the microwave power. X-mode launch, however, creates a "current clamp" during the ECH-on time which is released as soon as the microwave power is removed. This behavior varies with ECH power as shown in Fig. 14(a). The average current ramp rate during the microwave pulse is plotted as a function of ECH power for both X- and O-mode launch. The cyclotron resonance for all shots is located on axis. The O-mode current ramp rate is seen to increase asymptotically with power to *~1MA/s*. The maximum current ramp rate is reached at $P_{ECH} = \sim 50kW$, above which additional ECH power has little effect. This threshold of *50kW* was seen consistently for O-mode launch during all of TCA/ECH operation. X-mode launch reaches the same maximum as O-mode launch but at a lower power of $P_{ECH} = \sim 25kW$. As the ECH power increases from this point, the X-mode current ramp rate degrades. At high power the current clamping effect becomes clearly evident as seen in Fig. 13 and the high power X-mode points of Fig. 14(a). This behavior is consistently seen throughout these experiments.

The formation of the initial plasma current channel during startup is strongly affected by the location of ECH breakdown. We see this in Fig. 15(a) which plots the average plasma current ramp rate as a function of the measured position of the

current centroid *10ms* after the ECH turn-on for *~50* startup shots. These shots include variations in ECH power and gas injection. All shots have a central cyclotron resonance. The figure shows all shots starting to the LFS of the TCA poloidal cross section - a result of ECH breakdown to the LFS of the cyclotron resonance as seen in Fig. 9. This is contrary to standard ohmic cases which generally start on the HFS of the poloidal cross section. We also see in Fig. 15(a) a strong correlation between the position of the initial current centroid and the current ramp rate - shots with large x_p experiencing significantly lower ramp rates than shots with small x_p. Here, x_p is the normalized horizontal position of the current centroid. Generally, as the ECH power or prefill pressure is increased, the current centroid moves with the breakdown location to the LFS. The distribution of the startup current position for the shots of Fig. 15(a) is shown in Fig. 15(b) for X- and O-mode launch. We clearly see the more central startup accompanying O-mode launch where current ramp rates are highest. We assume that this is due to the more central and less localized breakdown profiles of O-mode power. It is important to note that X-mode points which do start more centrally, exhibit the same current ramp rates as O-mode points at the same radial location. This implies that the radial location of startup is more important in determining the current ramp rate than effects specific to either of the modes individually.

The decreased current ramp rates for currents located at larger major radius is thought to be due to a combination of several factors. Since the toroidal electric field, E_ϕ, varies as R^{-1}, a weaker driving force is applied for currents located at larger x_p. For TCA dimensions, E_ϕ is *30%* lower at the LFS limiter than on axis. Also, the vertical field (B_V) feedback system is set for central plasma positioning creating a vertical field roughly proportional to $I_p(x_p+c)$ where c is a constant producing the vertical field necessary to keep a centered plasma from drifting to the LFS. Therefore a plasma current created off axis is subjected to a $\vec{j} \times \vec{B_V}$ force which tries to sweep it out of its initial formation location creating a current profile center which no longer corresponds to the ECH energy deposition location. Error magnetic fields

may also result in decreased current ramp rates at large x_p. The field-line wall connection length, L_c, varies as:

$$L_c = d \frac{B_\phi}{B_{error}} \tag{4}$$

where B_ϕ is the applied toroidal field, B_{error} is the transverse error field, and d is the distance to the limiter in the poloidal plane along the error field. The distance d is a function of breakdown position, decreasing as the breakdown approaches the edge of the poloidal cross section. We see then that the decrease in dI_p/dt with x_p may partly be a result of decreased L_c and therefore of increased wall losses at large x_p. In TCA, we are unable to determine the magnitude of the error magnetic fields and therefore unable to estimate typical loss times associated with such fields. We do know that some moderate error field exists as we observe small toroidal currents ($100A$-$300A$) for low-density $V_L = 0V$ discharges which are known to accompany non-zero stray vertical fields [22, 23].

We can also attribute some of the decreased dI_p/dt with increasing x_p to the increased plasma inductance inherent to plasmas located at large x_p. The coaxial model of toroidal plasmas gives the plasma inductance as:

$$L_{tot} = L_{ext} + L_{int} = \mu_0 R \, ln\left(\frac{b}{a}\right) + \frac{\mu_0 R}{2} l_i \tag{5}$$

where L_{ext} = plasma external inductance, L_{int} = plasma internal inductance, a = plasma minor radius, b = average minor radius of the poloidal field windings, R = plasma major radius, l_i = normalized plasma inductance, and μ_0 = free-space permeability. An increase in x_p results in an increase in L_{tot} as $R = R_0 + a_0 x_p$, $a = a_0(1 - |x_p|)$, and $b = b_0 + a_0 x_p$ where R_0, a_0, b_0 are values for a plasma centered in the poloidal cross-section (i.e. $x_p = 0$). The normalized inductance, l_i, is taken from startup Thomson scattering measurements to be ~ 1.0 (measured at the end of

the ECH startup pulse). A choice of l_i for $0.5 < l_i < 1.5$ makes no significant difference in the following computations as the external inductance is the major contributor to the total inductance. An increase in x_p has relatively little effect on L_{int}, however, L_{ext} doubles as x_p moves from $x_p = 0$ to $x_p = 0.3$ and the total inductance more than doubles as x_p moves from $x_p = 0$ to $x_p = 0.5$. This change of L_{tot} with x_p can have a significant effect on the plasma current ramp rate. Here we calculate this effect for the highest power X- and O-mode shots of Figs. 14. We assume that the O-mode startup, being quite central, does not experience the current-limiting effects discussed in the previous paragraph, whereas the X-mode startup, taking place far to the LFS, does experience these effects as well as a reduced current ramp rate due to increased inductance. Using the Poynting formulation for the plasma power balance, we have:

$$V_L = V_{res} + \frac{1}{I_p}\frac{d}{dt}\left(\frac{1}{2}L_{tot}I_p^2\right) \tag{6}$$

where L_{tot} is given by Eq. 5. V_{res} then is the resistive contribution to the measured loop voltage and $\frac{1}{I_p}\frac{d}{dt}\left(\frac{1}{2}L_{tot}I_p^2\right)$ is the inductive contribution. Since we measure $V_L(t)$, $I_p(t)$, and all quantities required to calculate $L_{tot}(t)$ (from Eq. 5), we can perform the time derivative in Eq. 6 and calculate $V_{res}(t)$ for the $P_{ECH} = 100kW$, O-mode startup shot of Figs. 14. $V_{res}(t)$ is thus calculated and on average is $0.3V_L$ during the startup portion of the discharge. Assuming for simplicity that the resistive loop voltage is approximately the same for X- and O-mode startup at equal ECH power, we can compute the current ramp for the X-mode startup case ($P_{ECH} = 100kW$) accounting *only* for the effect of increased plasma inductance with increased x_p. We will refer to this as inductance-limited startup, $I_{ind}(t)$, and is computed numerically as the solution of:

$$\frac{dI_{ind}}{dt} + \frac{1}{2L_{tot}(t)} \frac{dL_{tot}}{dt} I_{ind}(t) - \frac{V_L(t) - V_{res}(t)}{L_{tot}(t)} = 0 . \qquad (7)$$

The inductance $L_{tot}(t)$ has been recalculated from measurements for the X-mode shot. The result is shown in Fig. 16. Figure 16(a) shows the measured current for the highest power X- and O-mode shots of Figs. 14 (solid) and the calculated current for inductance-limited X-mode startup computed with Eq. 7 (dashed). The difference in the currents between the inductance-limited X-mode and measured O-mode curves arises from the difference in the total inductance between the two measured cases, shown in Fig. 16(b). At the end of the ECH pulse, the X-mode inductance is seen to be twice that of the O-mode case, due the extreme shift of the plasma current to the LFS with X-mode launch. When the ECH is removed, the X-mode plasma current channel moves back to the center ($x_p=0$) and its inductance falls to that of the O-mode case. The current ramp rates then become approximately equal. The dashed curve therefore represents how the X-mode current ramp would appear if only the changing plasma inductance with X-mode launch were responsible for changing the current ramp rate. The increased X-mode inductance then accounts for about one-half of the difference in the measured current ramp rates for the X- and O-mode startup cases. We therefore must conclude that the other half is attributable to the effects of the toroidal electric field, vertical field feedback, and wall connection lengths, discussed earlier. We should also mention that the q values of these startup plasmas are too high (typically above $q = 50$) to explain the decreased current ramp rate at increased x_p by a plasma-position-dependent, low-q MHD current limit.

The current center position for the power series of Fig. 14(a) is plotted in Fig. 14(b). As the X-mode power increases, the current center is seen to move further and further to the LFS where the startup, as shown in Fig. 15(a) is poor. We see that increasing the O-mode power also causes a movement of the current center to the LFS. However, the displacement is small and does not cause a degradation of

the startup current ramp rate. Electron density profiles are shown in Figs. 17 for the $P_{ECH} = 20kW$ and $P_{ECH} = 100kW$ cases of Fig. 14 with the values averaged over the first $10ms$ of the discharges. We see that at $P_{ECH} = 20kW$ the O-mode launch density profile is nearly central while the X-mode launch profile already shows strong LFS peaking. As the power increases to $P_{ECH} = 100kW$, the O-mode profile also displaces somewhat to the LFS as n_e increases but still remains more central than the X-mode profile. Though the electron density profile measurements do not provide a spatial resolution as great as the H_α camera, the general shape of the density profiles is consistent with stronger X-mode LFS absorption. The measurement error shown in the figure is the absolute error of the measurement, limited by the resolution of the fringe shift measurement of the microwave interferometer. The relative error between measurements is much smaller and therefore the profile shape, the important aspect of these plots, is quite accurately represented.

The data presented in this section demonstrates that over the TCA operating conditions under which the data was taken, O-mode launch, due to its breakdown characteristics, allows startup more centrally and more efficiently over a wider range of operating parameters than X-mode launch. We see this consistently for all regimes of operation in which gas injection schemes, ECH power, ECH pulse length, and loop voltage are varied. For all of these data, the toroidal magnetic field is set for a central cyclotron resonance, resulting in startup for all shots to the LFS of the tokamak center. The data suggest that if the toroidal magnetic field were lowered to displace the cyclotron resonance to the HFS of the center, the breakdown would become more central and the startup performance of X-mode at high power may increase above that of Fig. 14(a). This though would require the proper density profile to create a nearly central UH resonance layer. The applied vertical field is controlled to position the plasma at $x = 0$. This setting may be important in determining the startup current position for the maximum current ramp rate. The fact that X-mode reaches its maximum current ramp rate at lower power than O-mode

suggests that X-mode startup may be more efficient than O-mode startup with proper density control, choice of magnetic field and positioning. If the highest current ramp rates for the lowest ECH power are required; these data suggest possible scenarios to effect the most efficient startup. This might involve decreasing the magnetic field to place the cyclotron resonance far to the HFS (but still with $x\omega ce > -1$) and preprogramming the position control to the expected breakdown location for the initial part of the pulse, switching to position feedback for central current position once a threshold current has been reached. Another possible scenario would require low-power microwave launch in the beginning of the shot to keep the density low and the breakdown central, increasing the power as the current rises and the absorption location becomes less critical. If, however, the flexibility or ease of tokamak operation is of primary importance, these data suggest that O-mode launch is more desirable than X-mode launch, allowing efficient startup over a wider range of operating conditions (i.e. B_ϕ, n_e, P_{ECH}, P_{fill}). O-mode launch also allows for easier LFS injection - a launch position not advisable with X-mode launch at the first harmonic.

We have several remarks relating to the operation of TCA during the experiments described in this paper. We generally operate with a loop voltage of $V_L = 2.0V$ ($E_\phi \sim 0.5V/m$). We are however able to achieve O-mode startup down to $V_L = 0.6V$ ($E_\phi \sim 0.15V/m$). This reduction in loop voltage, though, results in significantly reduced current ramp rates as shown in Fig. 18.

Prefill pressures used for these experiments range from $0.5x10^{-5}Torr < P_{fill} < 4x10^{-5}Torr$ with a typical value of $P_{fill} = 3x10^{-5}Torr$. Generally, as the fill pressure increases the current ramp rate decreases as the power per particle decreases and the current startup moves further to the LFS with the increasing density. Though the prefill pressure is controlled in every shot, we sometimes find it difficult to reproduce startup current ramp rates even at constant applied P_{fill}. This is due to the contribution of neutral particles recycled from the

walls which changes with wall conditioning, previous shot history, etc. This in part accounts for the scatter of points in x_p in Fig. 15(a). It should be noted that no wall conditioning is performed between shots.

The ECH power is reflected from an ellipsoidal microwave mirror, steerable both poloidally and toroidally. The range of possible toroidal injection angles is $-25° < \Theta_T < +25°$, where Θ_T is the angle between the beam path and the radial. As shown in Sec. IIIB the breakdown characteristics of neither X- nor O-mode launch change significantly when Θ_T is varied. We therefore do not expect and do not observe any change in the startup characteristics of either mode as we vary the toroidal injection angle over its entire range. This was tested in a variety of conditions.

V. Conclusions

The results that we have presented here are the result of a study designed specifically to compare the differences between X- and O-mode launch for ECH breakdown and startup in tokamak plasmas. We see spatially and temporally-resolved evidence of breakdown at both the cyclotron and UH resonance layers. Breakdown with X-mode launch is characterized by good first-pass absorption taking place only at the UH resonance layer. This absorption is well localized vertically. O-mode launched microwave power, however, is absorbed at both the cyclotron and UH resonance layers therefore distributing its power along the major radius. The low first-pass absorption results in a distributed vertical power deposition profile, as well, as the power reflects from the vessel walls. These reflections also result in mode mixing evidenced by breakdown at the UH layer, expected only for X-mode polarization. X-mode launch, in general, produces higher overall densities and a more prompt density rise than O-mode launch. The lower densities created by O-mode launch result in a smaller displacement of the UH

resonance layer to the LFS of the cyclotron resonance layer. This produces a more central breakdown than with X-mode launch whose power is absorbed far to the LFS. These breakdown characteristics are seen to affect the startup of TCA plasmas. The initial current ramp rate is strongly correlated with the startup current position - currents starting at larger major radius experiencing significantly lower current ramp rates. Increasing plasma external inductance with increasing major radius accounts for part of the decreased current ramp rate. The remainder is thought to be due to lower toroidal electric fields and lower field line connection lengths for plasmas located at large R, and the vertical field feedback designed for central plasma positioning which attempts to move the plasma radial position away from the location of the ECH power deposition. O-mode launch is seen to start more centrally than X-mode launch resulting in higher current ramp rates. X-mode launch creates the initial plasma current far to the LFS of the tokamak poloidal cross section resulting in a degraded startup performance. This effect becomes more pronounced at high powers, a result of the increasing n_e with P_{ECH} and subsequent displacement of the UH resonance layer further to the LFS. The movement of the current position with increasing power is also seen with O-mode launch, however the effect is much smaller due to breakdown at the fixed cyclotron resonance and a smaller Δx_{UH}. The data suggest that with careful control of the toroidal magnetic field, electron density, and position feedback, X-mode launch may result in more efficient startup. O-mode launch, though, is seen to provide efficient startup over a wider range of operating parameters.

Acknowledgements

We would like to thank Dr. A. Pietrzyk for his work on Thomson scattering measurements, Dr. M. Dutch for his work on NPA measurements, as well as

acknowledge the support of the TCA and gyrotron teams. This work was partly supported by the Fonds National Suisse de la Recherche Scientifique.

X- and O-Mode ECH Breakdown and Startup in TCA

References

[1] BULYGINSKII, D. G., LARIONOV, M. M., LEVIN, L. S., MIKLUKHO, O. V., A. I. TOKUNOV, SHUSTOVA, N. V., Sov. J. Plasma Phys. **6** (1980) 11.

[2] CHO, T., KUBO, S., IKEDA, M., SAITO, T., TERUMICHI, Y., HAMADA, Y., TANAKA, S., Phys. Lett. **77A** (1980) 318.

[3] GILGENBACH, R. M., READ, M. E., HACKETT, K. E., LUCEY, R. F., GRANATSTEIN, V. L., ENGLAND, A. C., LORING, C. M., WILGEN, J. B., ISLER, R. C., PENG, Y-K. M., BURRELL, K. H., ELDRIDGE, O. C., HACKER, M. P., KING, P. W., KULCHAR, A. G., MURAKAMI, M., RICHARDS, R. K., Nuc. Fusion **21** (1981) 319.

[4] KULCHAR, A. G., ELDRIDGE, O. C., ENGLAND, A. C., BUSH, C. E., EDMONDS, P. H., KELLY, G. G., LORING, C. M., PENG, Y-K. M., WILGEN, J. B., BOROWSKI, S. K., Phys. Fluids **27** (1984) 1869.

[5] LLOYD, B., EDLINGTON, T., Plasma Phys. and Contr. Fusion **28** (1986) 909.

[6] LLOYD, B., JACKSON, G. L., TAYLOR, T. S., LAZARUS, E. A., LUCE, T. C., PRATER, R., Nuc. Fusion **31** (1991) 2031.

[7] DOANE, J., Internat. J. Electronics **53** (1982) 573.

[8] LLOYD, B., EDLINGTON, T., ALCOCK, M. W., ATKINSON, D., PARHAM, B. J., COLLINS, P. R., DELLIS, A. N., RILEY, J., RIVIERE, A. C., ROBINSON, D. C., TODD, T. N., in Controlled Fusion and Plasma Physics (Proc. 13th Eur. Conf. Schliersee 1986) Vol. 10C, European Physical Society (1986) 266.

[9] CHEETHAM, A. D., HEYM, A., HOFMANN, F., HRUSKA, K., KELLER, R., LIETTI, A., LISTER, J. B., POCHELON, A., RIPPER, H., SIMIK, A., TUSZEL, A., in Fusion Technology (Proc. 11th Symp. on Fusion Tech. Oxford 1980) Vol. I, Pergamon Press (1980) 601; CHEETHAM, A. D., HEYM, A., HOFMANN, F., HRUSKA, K., KELLER, R., LIETTI, A., LISTER, J. B., POCHELON, A., RIPPER, H., SCHREIBER, R. SIMIK, A., The TCA Tokamak Project Report, CRPP Report LRP 162/80 (1980).

[10] HOLLENSTEIN, CH., DUVAL, B. P., DUDOK DE WIT, T., JOYE, B., KÜNZLI, H. J., OELHAFEN, P., ZEHRINGER, R., HAUERT, R., MOSER, E. M., J. Nuc. Mat. **176 & 177** (1990) 343.

[11] POCHELON, A., GOODMAN, T. P., WHALEY, D. R., TRAN, M. Q., PERRENOUD, A., REINHARD, D., JÖDICKE, B., MATHEWS, H. G., KASPAREK, W., THUMM, M., in Fusion Technology (Proc. 16th Symp. on Fusion Tech. London 1990) Vol. II, Elsevier Science Publishers B. V. (1991) 1075.

[12] ANISIMOV, A. I., VINOGRADOV, N. I., POLOSKIN, B. P., Sov. Phys. Tech. Phys. **18** (1973) 459.

[13] CHO, T., OGURA, K., ANDO, A., TANAKA, H., NAKAMURA, M., NAKAO, S., SHIMOZUMA, T., KUBO, S., MAEKAWA, T., TERUMICHI, Y., TANAKA, S., Nuc. Fusion **26** (1986) 349.

[14] SCHUSS, J. J., HOSEA, J. C., Phys. Fluids **18** (1975) 727.

[15] CHANG, R. P. H., PORKOLAB, M., GREK, B., Phys. Rev. Lett. **28** (1972) 206.

[16] OKABAYASHI, M., CHEN, K., PORKOLAB, M., Phys. Rev. Lett. **31** (1973) 1113.

[17] PORKOLAB, M., ARUNASALAM, V., LUHMANN, N. C. JR., SCHMITT, J. P. M., Nuc. Fusion **16** (1976) 269.

[18] MCDERMOTT, F. S., BEKEFI, G., HACKETT, K. E., LEVINE, J. S., PORKOLAB, M., Phys. Fluids **25** (1982) 1488.

[19] BULYGINSKII, D. G., GUSEV, V. K., DJACHENKO, V. V., IRZAK, M. A., KANTOR, M. YU., LARIONOV, M. M., LEVIN, L. S., SEREBRENY, G. A., SHUSTOVA, N. V., in Controlled Fusion and Plasma Physics (Proc. 11th Eur. Conf. Aachen 1983) Vol. 7D, European Physical Society (1983) 457.

[20] ANISIMOV, A. I., VINOGRADOV, N. I., POLOSKIN, B. P., Sov. Phys. Tech. Phys. **20** (1975) 629.

[21] CARDINALI, A., ROMANELLI, F., Joint Varenna-Lausanne Int. Workshop on Theory of Fusion Plasmas, Varenna 1990, edited by E. Sindoni, F. Troyon, and J. Vaclavik, Editrice Compositori, Bologna, Italy (1990) 437.

[22] POLMAN, R. W., VAN ANDEL, R., BOSMAN, R., DAMSTRA, R., DA CRUZ JR., D. F., DE GROOT, B., HUGENHOLTZ, C. A. J., KONIG, J. J., KOOIJMAN, W., KRUYT, O. G., LOK, J., VAN MILLIGEN, B. PH., OOMENS, A. A. M., SCHÜLLER, F. C., SMITS, F. M. A., SMEETS, P. H. M., STAKENBORG, J., TIELEMANS, A. J. H., TITO, C. J., VERHOEVEN, A. G. A., WESTERHOF, E., in Controlled Fusion and Plasma Physics (Proc. 17th Eur. Conf. Amsterdam 1990) Vol. 14B, European Physical Society (1990) 1122 and references contained therein.

[23] CIRANT, S., ARGENTI, L., CIMA, G., MANTICA, P., MAROLI, C., PETRILLO, V., in Controlled Fusion and Plasma Physics (Proc. 15th Eur. Conf. Dubrovnik 1988) Vol. 12B, European Physical Society (1988) 831.

X- and O-Mode ECH Breakdown and Startup in TCA

Figure captions

Figure 1. *39GHz* gyrotron and microwave line elements. The gyrotron outputs a TE_{02} beam with a mode purity of *98%*. The TE_{02} output is converted to the HE_{11} mode for X- or O-mode launch into TCA. Computed line efficiency is *90%* and HE_{11} cross polarization is measured to be $<1.5\%$.

Figure 2. TCA poloidal cross section including waveguide, quartz window, ellipsoidal microwave mirror, and transmission measurement antennas. The mirror is steerable allowing access to the region between the cross-hatched lines. Toroidal angles of $\pm 25^\circ$ to the radial are also possible.

Figure 3. Schematic of diagnostic chords showing a) TCA vacuum vessel b) plasma c) H_α camera d) microwave interferometer e) visible emission spectrometer. c, d, and e are used to measure power deposition profiles for X- and O-mode launch.

Figure 4. H_α contours for *10ms, 35kW*, O-mode launch ($V_L = 0V$). Computed positions of (A) the cyclotron resonance and (B', B'') the UH resonance, using measured B_ϕ and horizontal electron density profiles, are shown. Curve B' assumes a flat vertical density profile and B'' assumes a peaked vertical density profile. Shows spatial- and time-resolved absorption at both the cyclotron and UH resonances.

Figure 5. Transmission measurements for X-and O-mode launch for breakdown ($V_L = 0V$) and startup ($V_L = 2V$) discharges. All breakdown cases lie in the density range $\bar{n}_e < 3x10^{12}cm^{-3}$ where O-mode single pass absorption is seen to be poor. X-mode transmission is reduced to zero for all but zero density due to the UH resonance and R-cutoff lying in front of the X-mode receiving horn. The large error bars result from a central density measurement which does not account for off-axis

density peaking, leading to a spread in the measured transmission for equal measured central densities.

Figure 6. Vertical visible emission profiles for (a) X- and (b) O-mode launch (geometry shown in Fig. 3) for $V_L = 0V$. O-mode launch produces flat emission profiles indicating power spreading due to wall reflections after poor single-pass absorption. X-mode exhibits peaked profiles indicating localized absorption without spatial spreading due to wall reflections. This is an indication of good single-pass X-mode absorption. X-mode power is poorly absorbed on the first pass for the first $\sim 800\mu s$ before the initial plasma is formed.

Figure 7. Average electron density for X- and O-mode launch for varying B_ϕ ($V_L = 0V$). The profiles are measured using a five-channel microwave interferometer and densities are averaged over the $20ms$ microwave pulse ($P_{ECH} = 50kW$). X-mode launch is seen to produce 20%-40% higher average densities than O-mode. The total ionization capability for both modes is also seen to decrease as the magnetic field increases and the resonances move to the LFS.

Figure 8. (a) Carbon-IV burnthrough time for X- and O-mode launch for started discharges ($V_L = 2V$) with $\Delta t_{ECH} = 10ms$. Shows higher electron heating rates with X-mode launch.
(b) P_{rad}/n_e for same shots. Shows higher O-mode launch impurity levels at beginning of pulse resulting from higher O-mode wall loading. This effect is seen to disappear within $20ms$ of the current startup and does not affect the impurity concentration later in the discharge for startup with either mode.

Figure 9. Horizontal H_α emission profiles for X-mode launch (open circles) and O-mode launch (filled circles) at $P_{ECH} = 80kW$ and $V_L = 0V$. Each point shown represents a pixel of the H_α camera. O-mode launch exhibits absorption at the cyclotron resonance (HFS O-mode peak) and the UH resonance (LFS O-mode peak). X-mode launch exhibits absorption at only the UH resonance. The shift of the UH peak, Δx_{UH}, for X-mode launch is 50% larger than that for O-mode launch due to the higher densities created by X-mode launch.

Figure 10. Neutral particle analyzer data for an X-mode, $P_{ECH} = 120kW$ breakdown shot. Shows ion heating during the ECH pulse. (a) ECH power (b) electron density - central chord (c) NPA count rate at (1) $1080eV \pm 50eV$ (2) $1440eV \pm 90eV$ (3) $2100eV \pm 150eV$. This effect is seen over all breakdown densities and diminishes by at least a factor of ten when the launch is changed from X- to O-mode.

Figure 11. Horizontal H_α emission profiles for X-mode launch at $\Theta_T = 0°$ (open circles) and $\Theta_T = 25°$ (filled circles) at $P_{ECH} = 80kW$ and $V_L = 0V$. The emission profiles are identical with the exception of the region around the cyclotron resonance where slightly higher absorption is seen for the $\Theta_T = 25°$ case. This is a small, though reproducible effect.

Figure 12. Typical ECH-assisted startup scenario. The microwave pulse is typically delayed from the V_L turn-on time to avoid the $4V$ spike that occurs at the beginning of the V_L pulse. No plasma is created during this delay interval. A prompt density rise and current ramp accompanies the microwave turn-on. The line-averaged density trace shown is for the chord which passes through the center of the plasma cross-section. The microwave power for the discharge is launched in O-mode at $P_{ECH} = 60kW$, $\Delta t_{ECH} = 40ms$.

Figure 13. Current ramp for ECH-assisted startup for X- and O-mode launch at $P_{ECH} = 100kW$, $\Delta t_{ECH} = 10ms$. X-mode launch is seen to produce a clamping of the current, delaying the current rise until after the ECH power has been removed. The cyclotron resonance is located on axis.

Figure 14. (a) Average plasma current ramp rate during $10ms$ ECH startup pulses. O-mode is seen to perform at its maximum ($dI_p/dt \sim 1MA/s$) for $P_{ECH} > 50kW$. X-mode startup reaches this same maximum at $P_{ECH} = 25kW$ but performance degrades with higher ECH power. The cyclotron resonance is located on axis.
(b) Plasma current position at end of microwave pulse. With increasing power, startup with X-mode launch shifts to the low field side where startup is poor.

Figure 15. (a) Average current ramp rate over $10ms$ ECH startup pulse vs. startup current position. The current is seen to start to the low field

side of the cyclotron resonance and the current ramp rates decrease with increasing x_p.

(b) Distribution of startup current position for X- and O-mode startup. Shows O-mode launch results in a more central startup than X-mode launch where current ramp rates are higher. Also where X- and O-mode launch result in the same initial x_p, current ramp rates are similar.

Figure 16. (a) Measured X- and O-mode current for highest power shots of Figs. 14 (solid curves) and computed X-mode current accounting only for effects of increased plasma inductance with x_p (dashed curve). (b) ratio of L_{tot} for measured X- and O-mode startup cases of (a).

Figure 17. Density profiles for X- and O-mode launch at (a) $P_{ECH} = 20kW$ and (b) $P_{ECH} = 100kW$. O-mode launch consistently creates a more central density profile.

Figure 18. Current ramp rate dependence on toroidal electric field. Shows startup achievable at $E_\phi \geq 0.15V/m$. All shots have a central cyclotron resonance. Different symbols show data taken on three different days of operation.

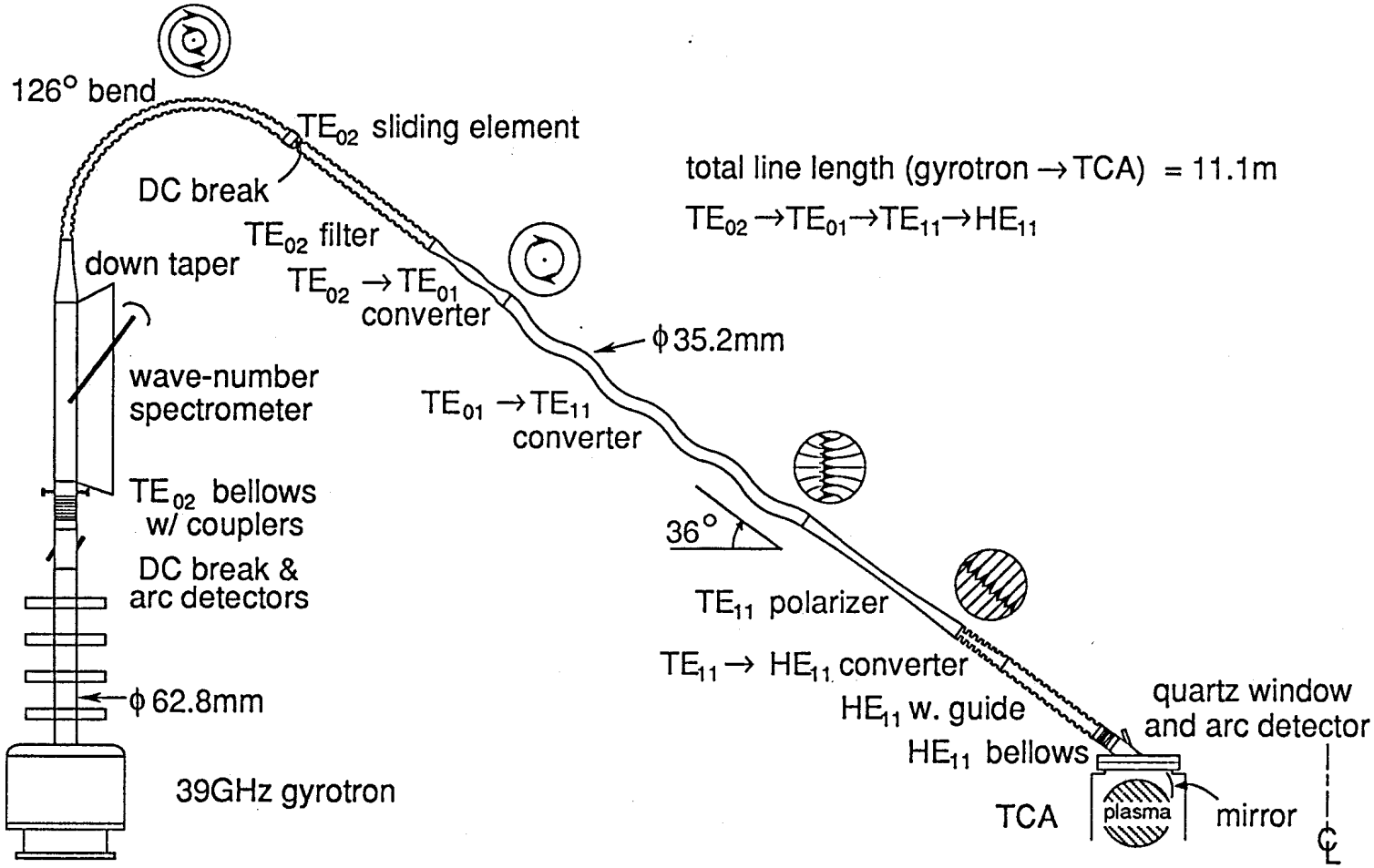
126° bend
TE02 sliding element
DC break
TE02 filter
down taper
TE02 → TE01 converter
total line length (gyrotron → TCA) = 11.1m
TE02 → TE01 → TE11 → HE11
ϕ35.2mm
wave-number spectrometer
TE01 → TE11 converter
TE02 bellows w/ couplers
36°
DC break & arc detectors
TE11 polarizer
TE11 → HE11 converter
ϕ62.8mm
HE11 w. guide
quartz window and arc detector
HE11 bellows
39GHz gyrotron
TCA
plasma
mirror

Figure 1

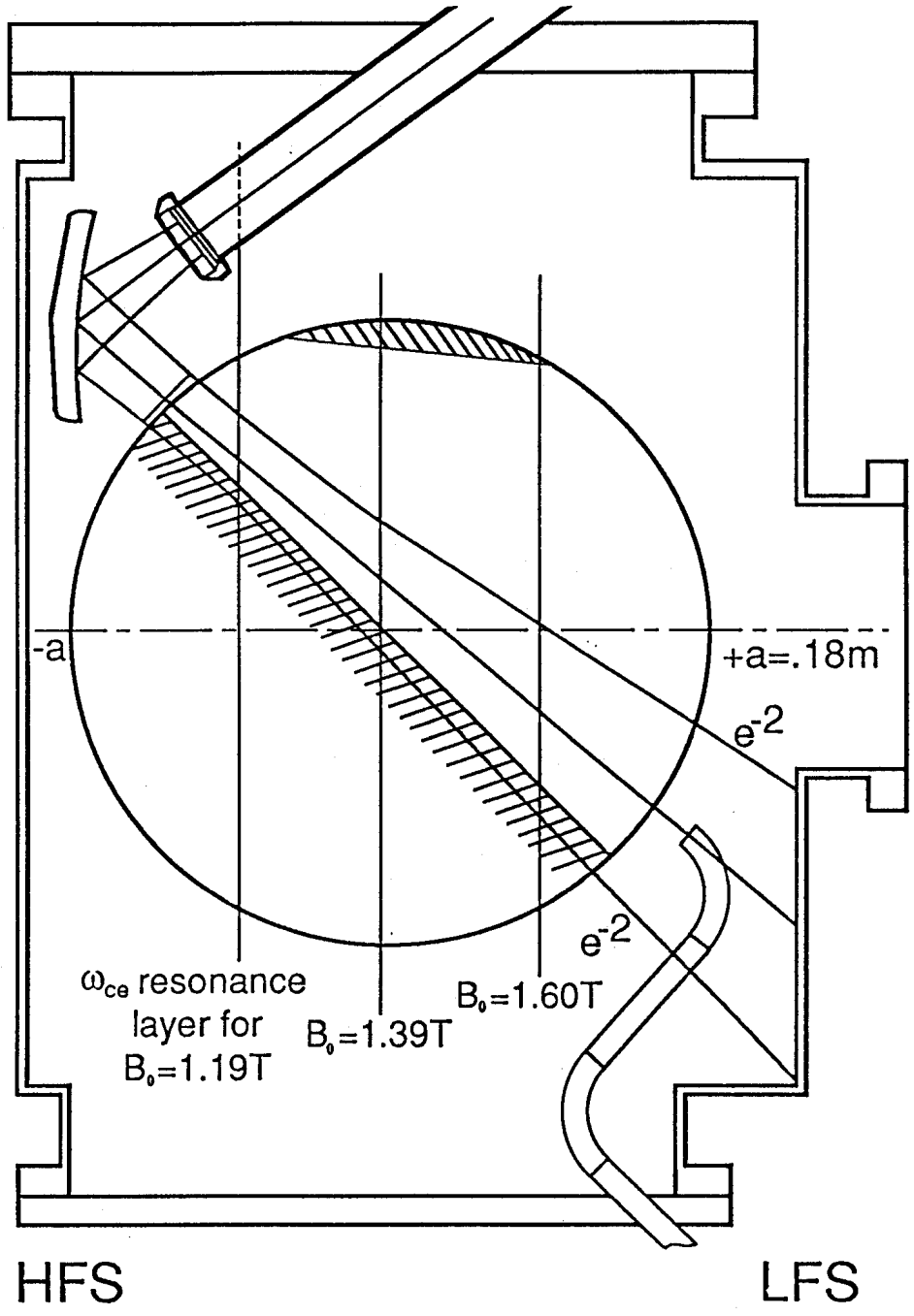
-a
+a=.18m
e-2
e-2
ωce resonance
layer for
B0=1.19T
B0=1.39T
B0=1.60T
HFS
LFS

Figure 2

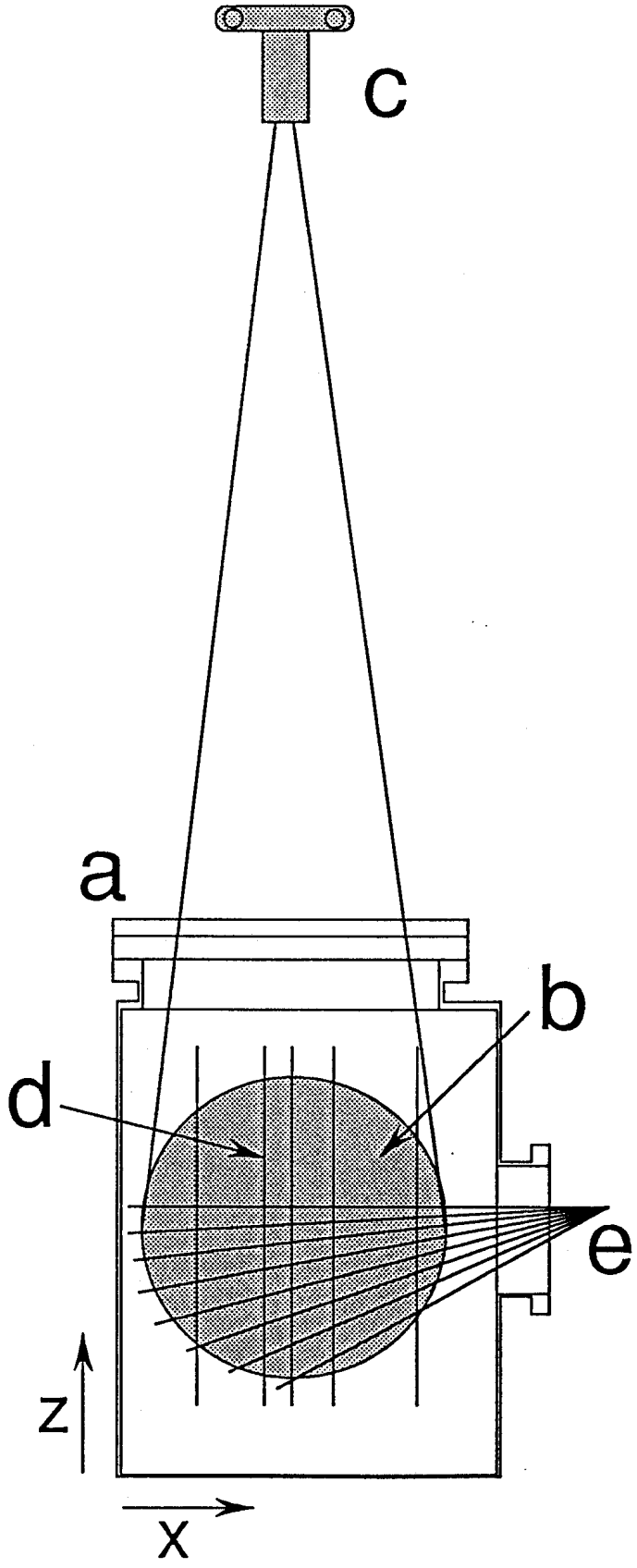

Figure 3

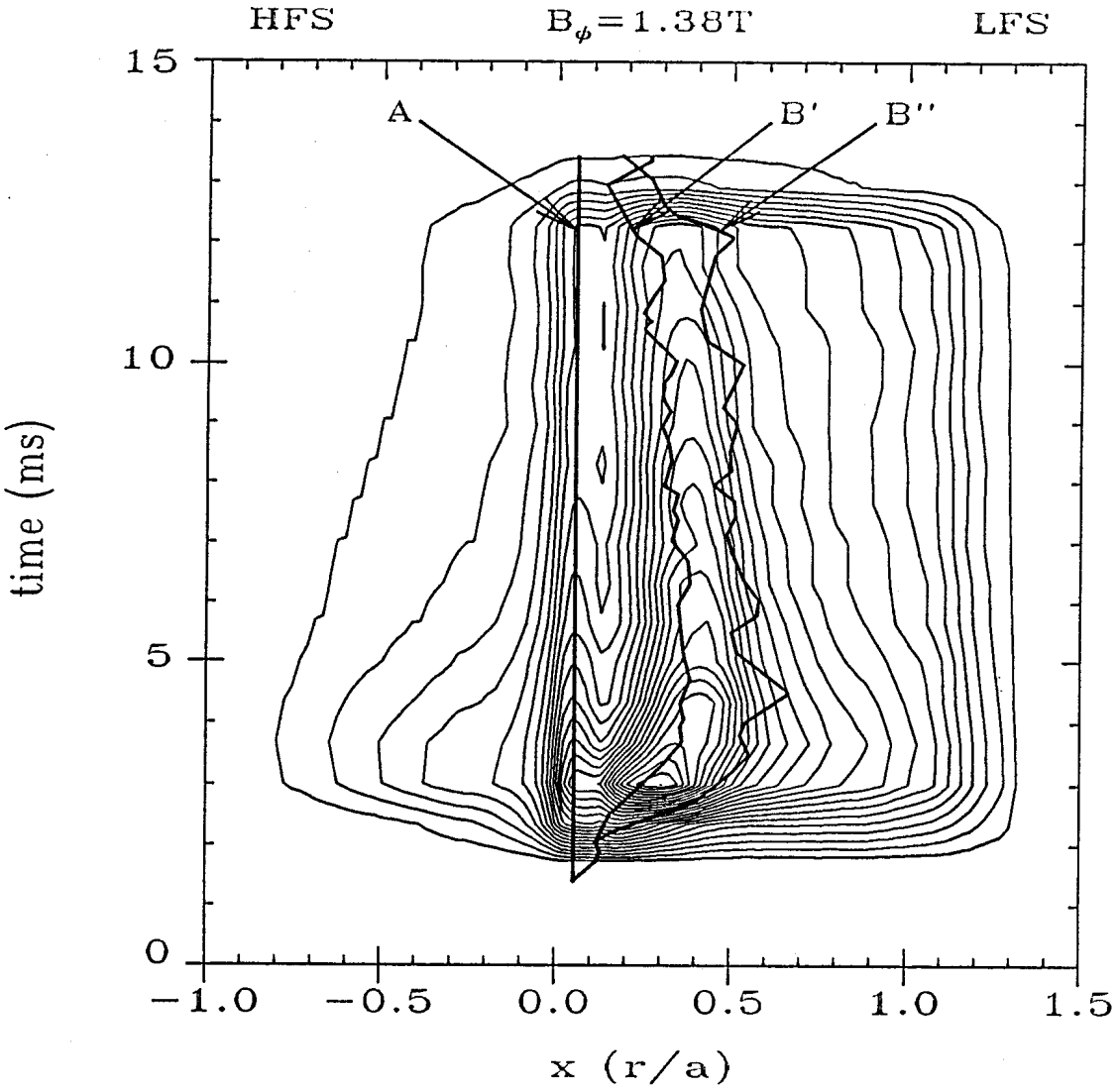

Figure 4

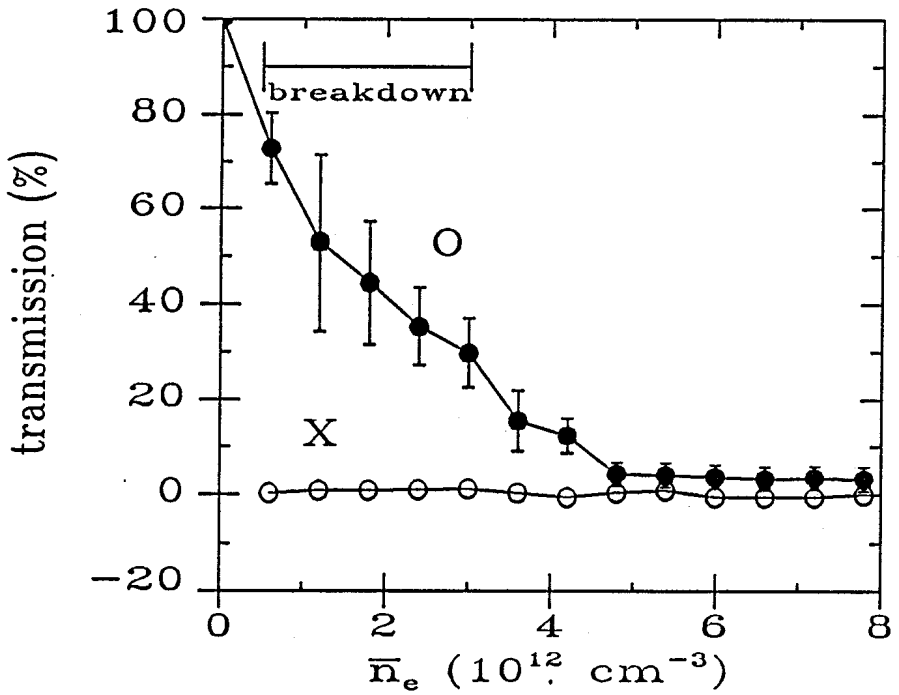
100
80
60
40
20
0
−20
transmission (%)
breakdown
O
X
0
2
4
6
8
$\bar{n}_e$ (10^{12} cm^{-3})

Figure 5

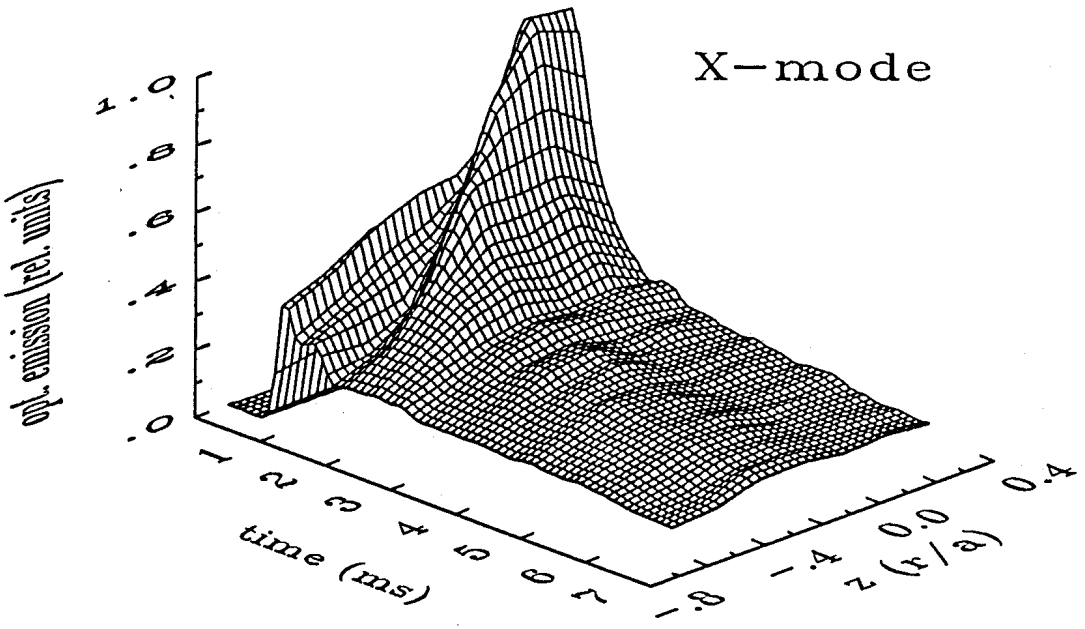
X-mode
opt. emission (rel. units)
1.0
.8
.6
.4
.2
.0
1
2
3
4
5
6
7
time (ms)
-.8
-.4
0.0
0.4
z (r/a)

Figure 6a

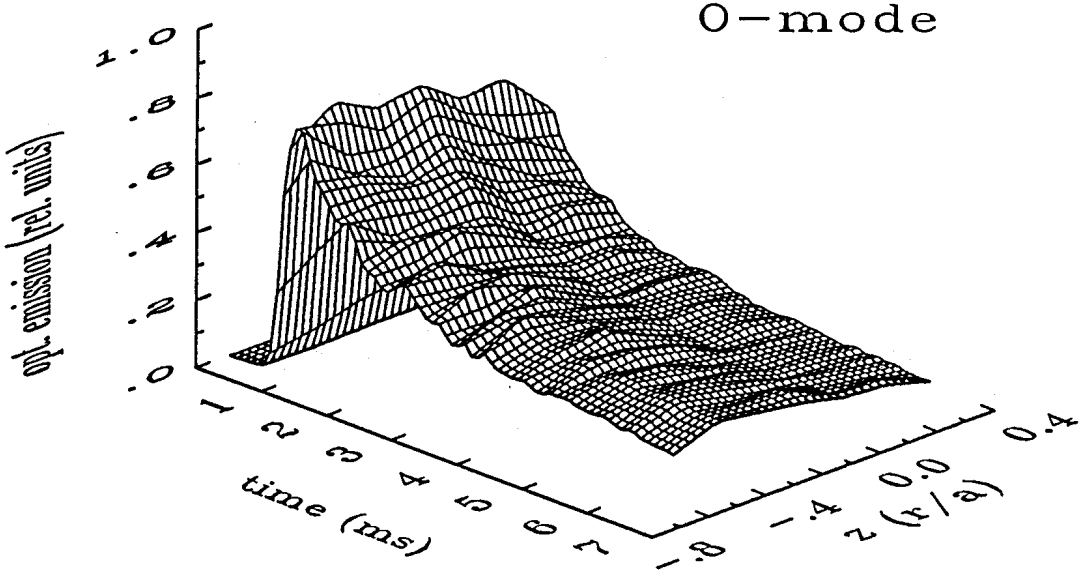
O-mode
opt. emission (rel. units)
1.0
.8
.6
.4
.2
.0
1
2
3
4
5
6
7
time (ms)
-.8
-.4
0.0
0.4
z (r/a)

Figure 6b

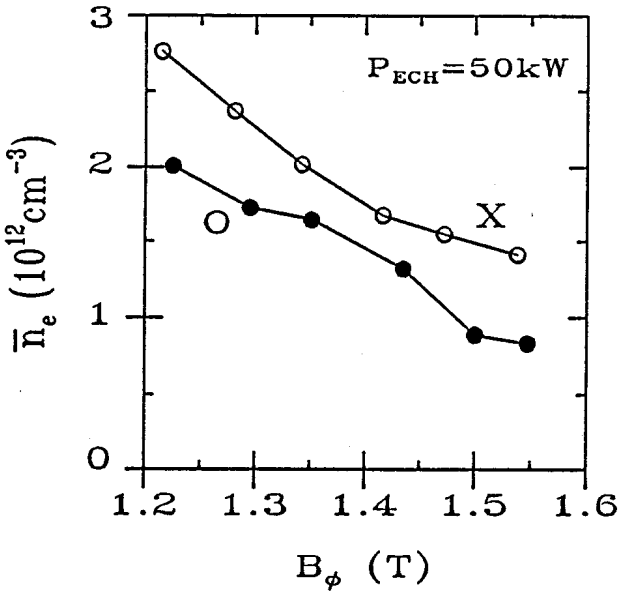

Figure 7

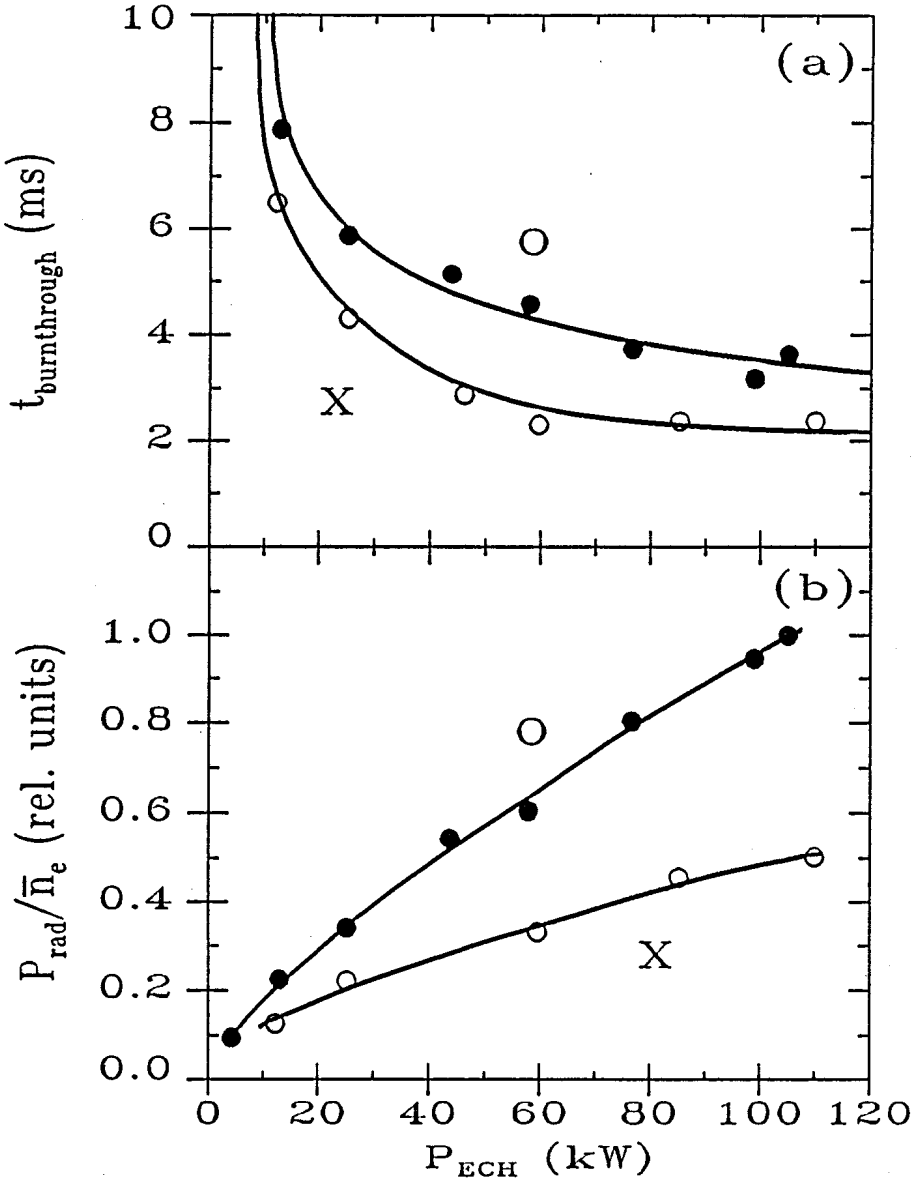
(a)
(b)
O
X
O
X
$t_{burnthrough}$ (ms)
$P_{rad}/\bar{n}_e$ (rel. units)
P_{ECH} (kW)
0
2
4
6
8
10
0.0
0.2
0.4
0.6
0.8
1.0
0
20
40
60
80
100
120

Figure 8

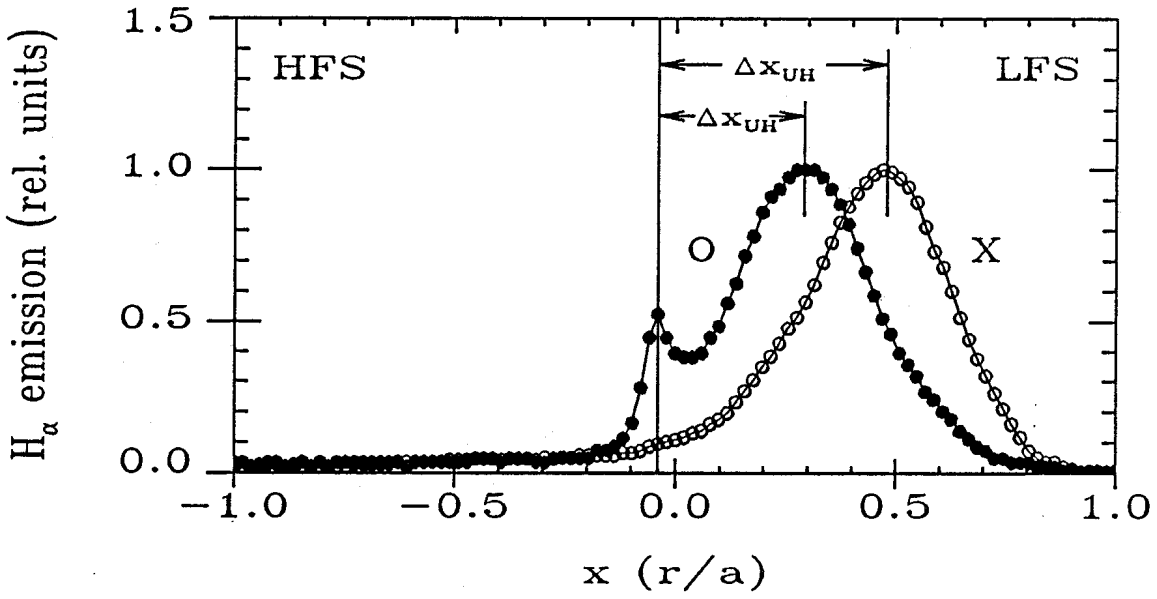
1.5
1.0
0.5
0.0
HFS
LFS
Δx_{UH}
Δx_{UH}
O
X
−1.0
−0.5
0.0
0.5
1.0
H_α emission (rel. units)
x (r/a)

Figure 9

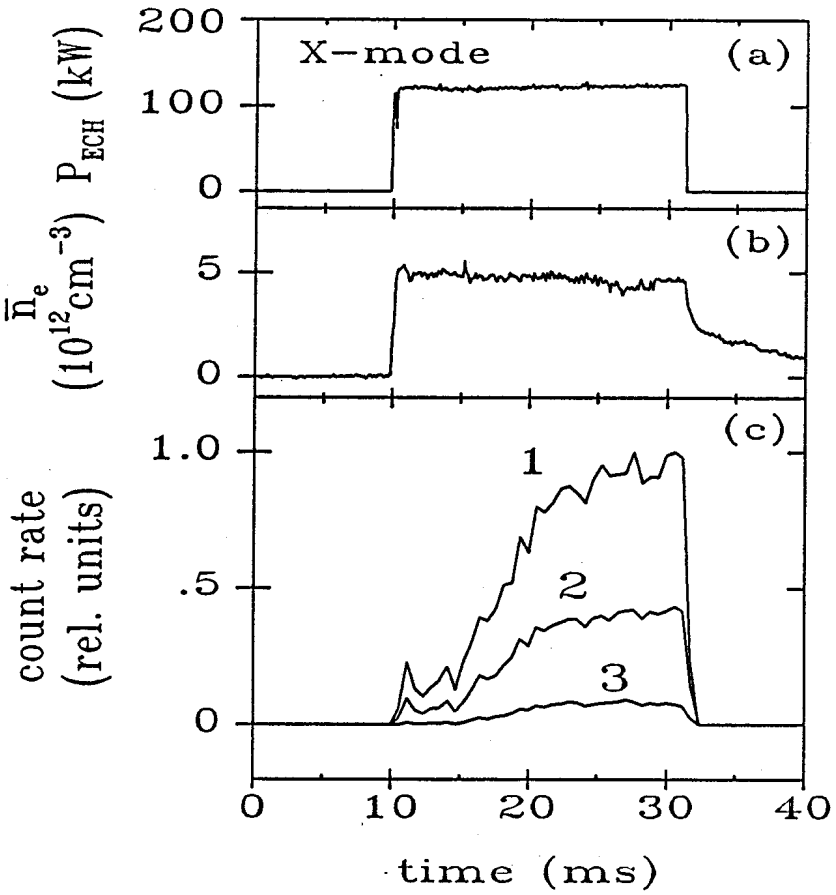
X-mode
(a)
(b)
(c)
200
100
0
5
0
1.0
.5
0
1
2
3
0
10
20
30
40
time (ms)
$\bar{n}_e$ (10^{12}cm^{-3})
P_{ECH} (kW)
count rate (rel. units)

Figure 10

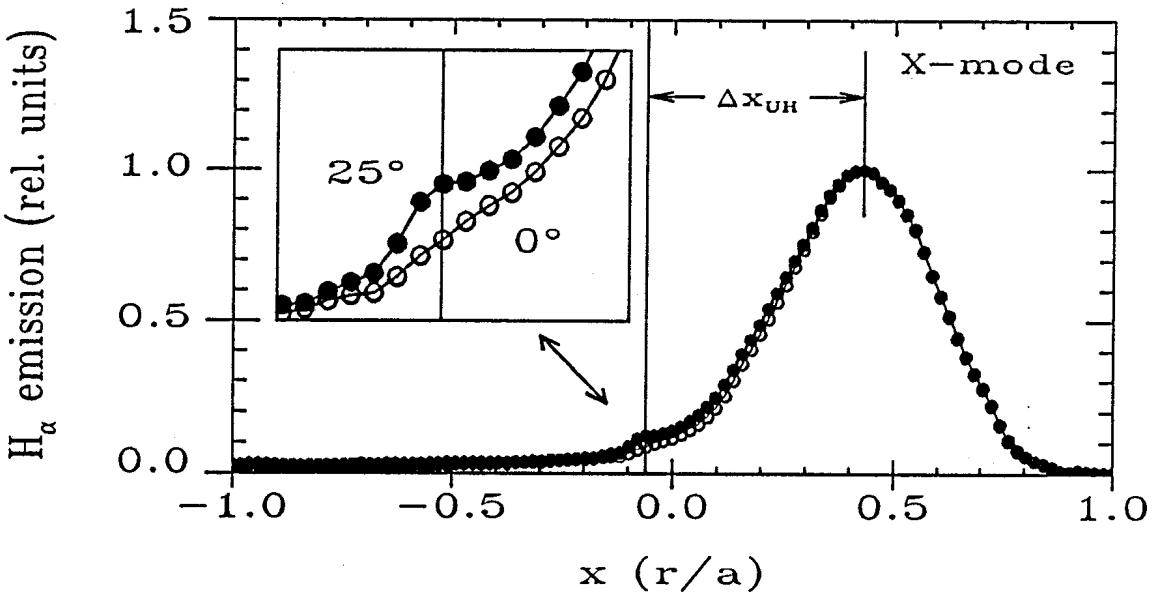
1.5
1.0
0.5
0.0
−1.0
−0.5
0.0
0.5
1.0
H_α emission (rel. units)
x (r/a)
25°
0°
Δx_{UH}
X−mode

Figure 11

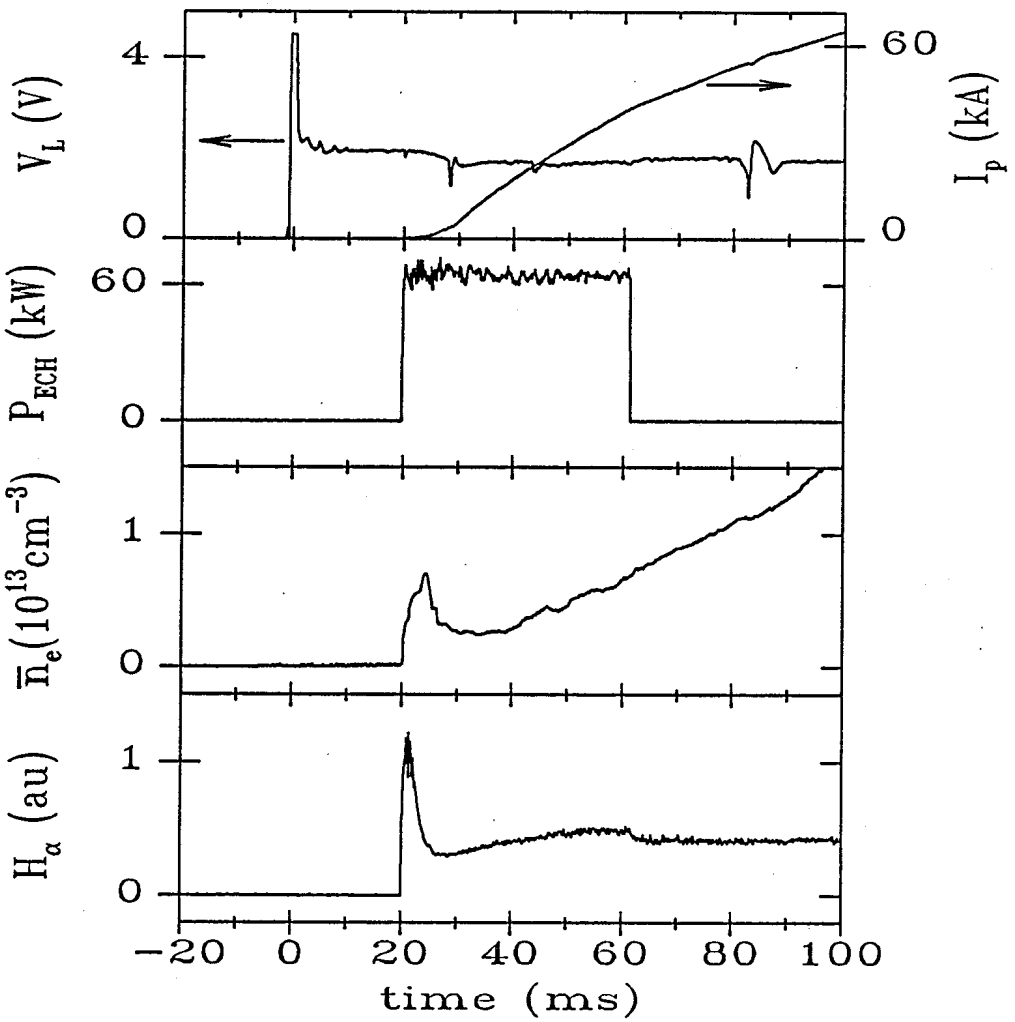
4
0
60
0
V_L (V)
I_p (kA)
60
0
P_{ECH} (kW)
1
0
$\bar{n}_e(10^{13}cm^{-3})$
1
0
H_α (au)
−20
0
20
40
60
80
100
time (ms)

Figure 12

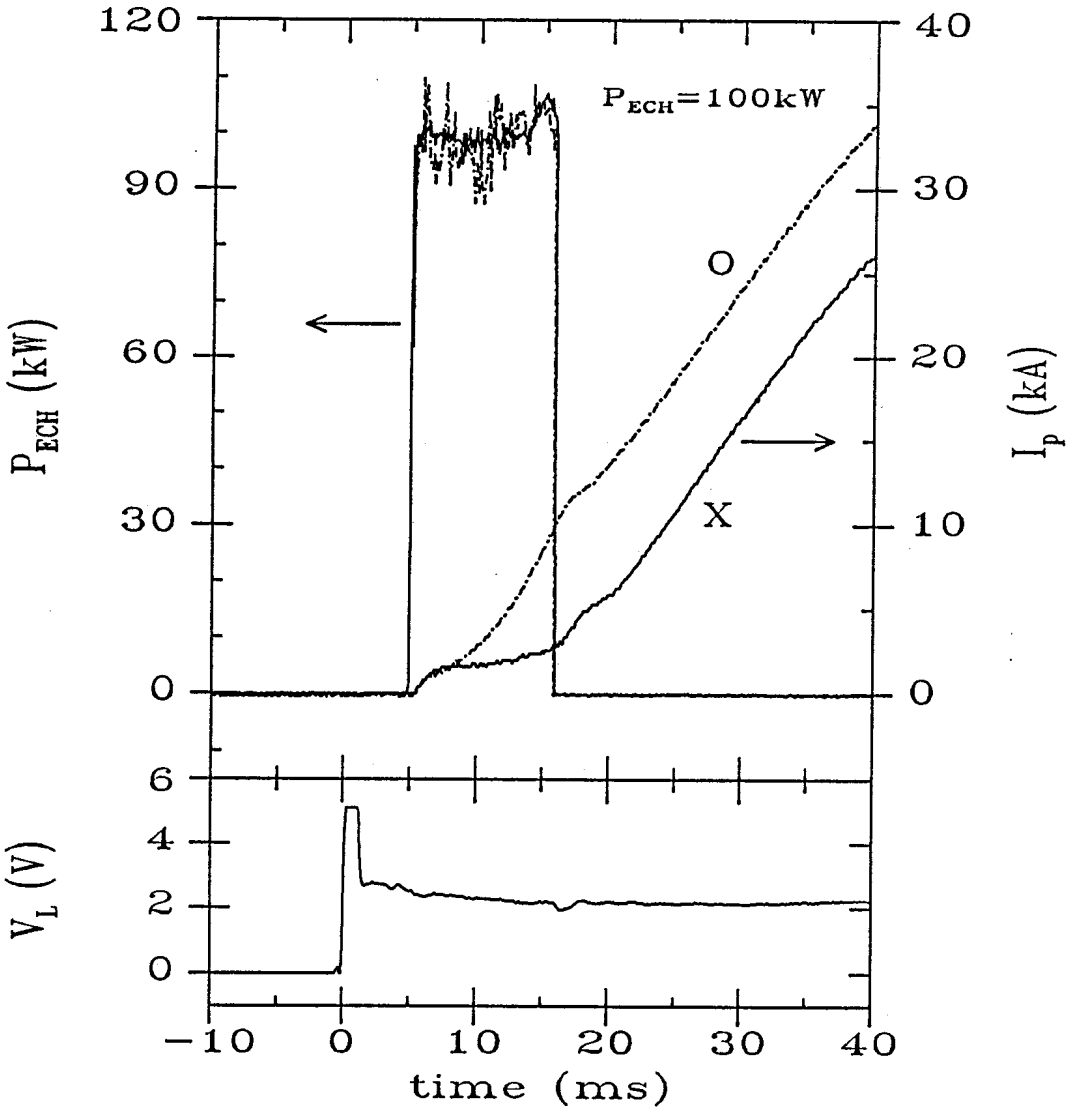
120
90
60
30
0
40
30
20
10
0
P_{ECH}=100kW
O
X
P_{ECH} (kW)
I_p (kA)
6
4
2
0
V_L (V)
−10
0
10
20
30
40
time (ms)

Figure 13

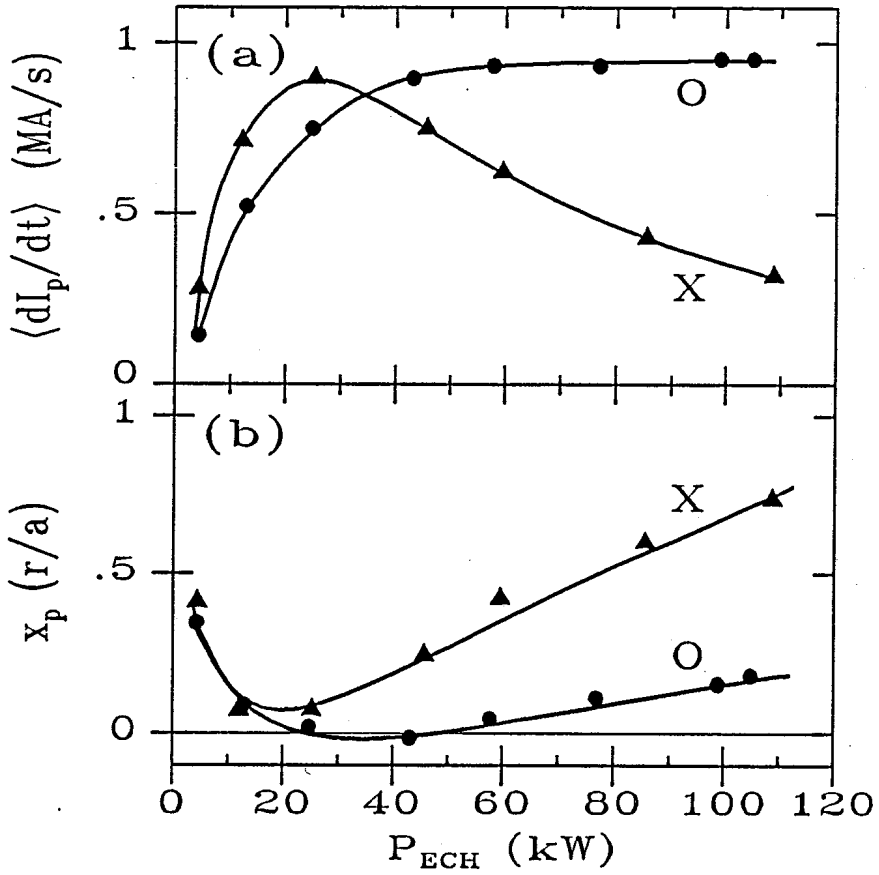
(a)
(b)
O
X
X
O
1
.5
0
1
.5
0
$\langle dI_p/dt \rangle$ (MA/s)
x_p (r/a)
0
20
40
60
80
100
120
P_{ECH} (kW)

Figure 14

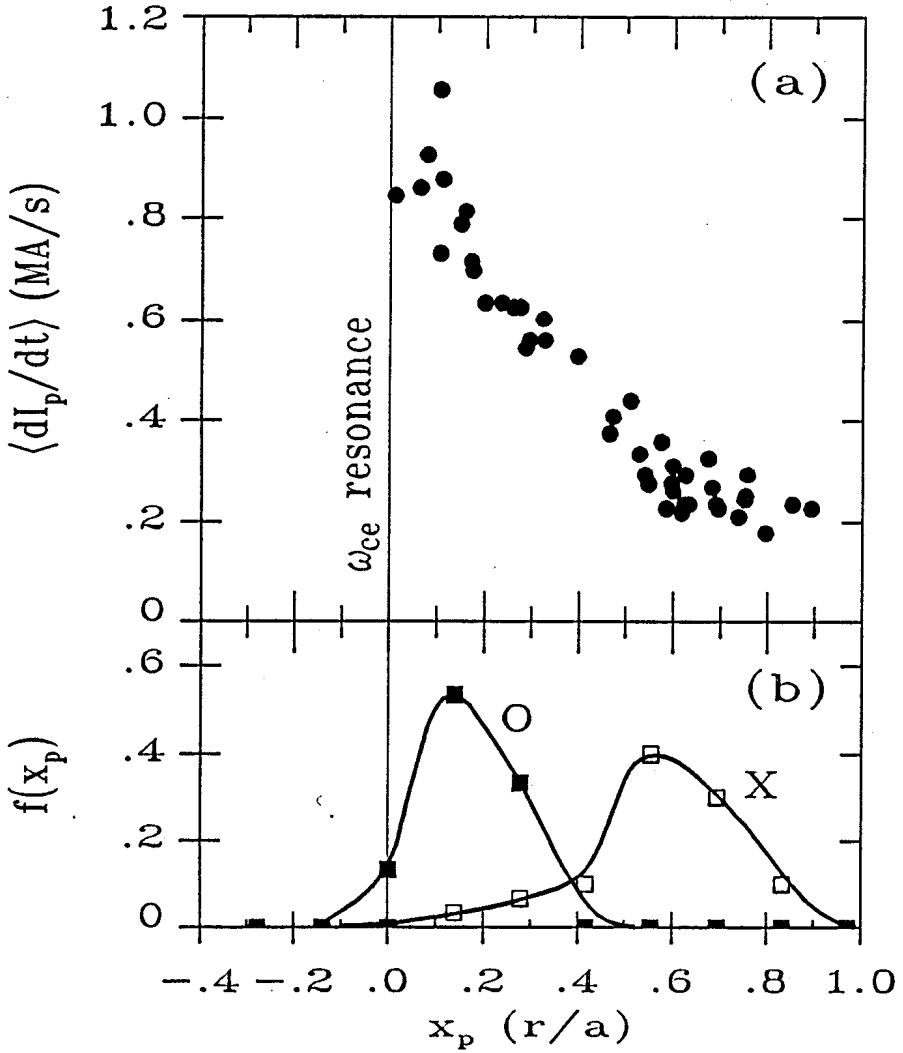
1.2
1.0
.8
.6
.4
.2
0
(a)
⟨dI_p/dt⟩ (MA/s)
ω_ce resonance
.6
.4
.2
0
(b)
O
X
f(x_p)
−.4 −.2 .0 .2 .4 .6 .8 1.0
x_p (r/a)

Figure 15

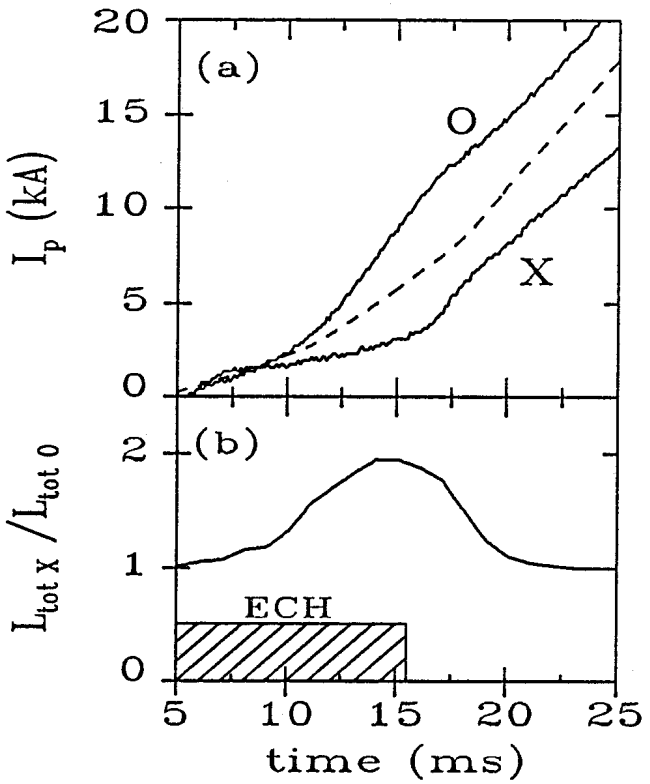

Figure 16

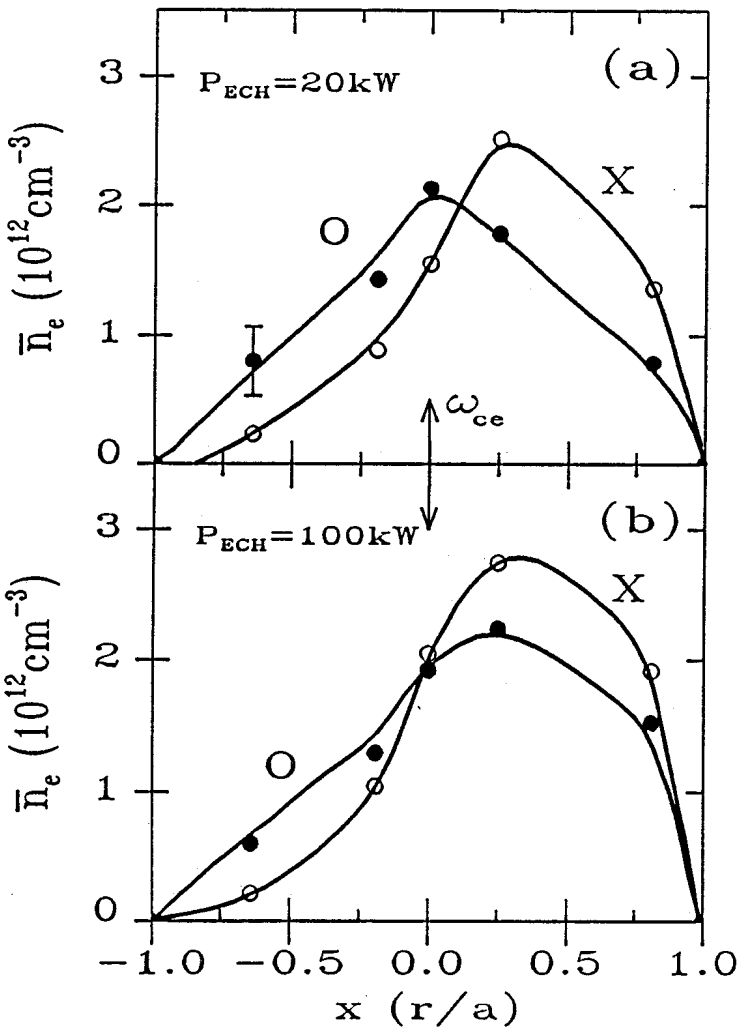
P_ECH=20kW
(a)
X
O
ω_ce
P_ECH=100kW
(b)
X
O
n̄_e (10^12 cm^-3)
n̄_e (10^12 cm^-3)
3
2
1
0
−1.0
−0.5
0.0
0.5
1.0
x (r/a)

Figure 17

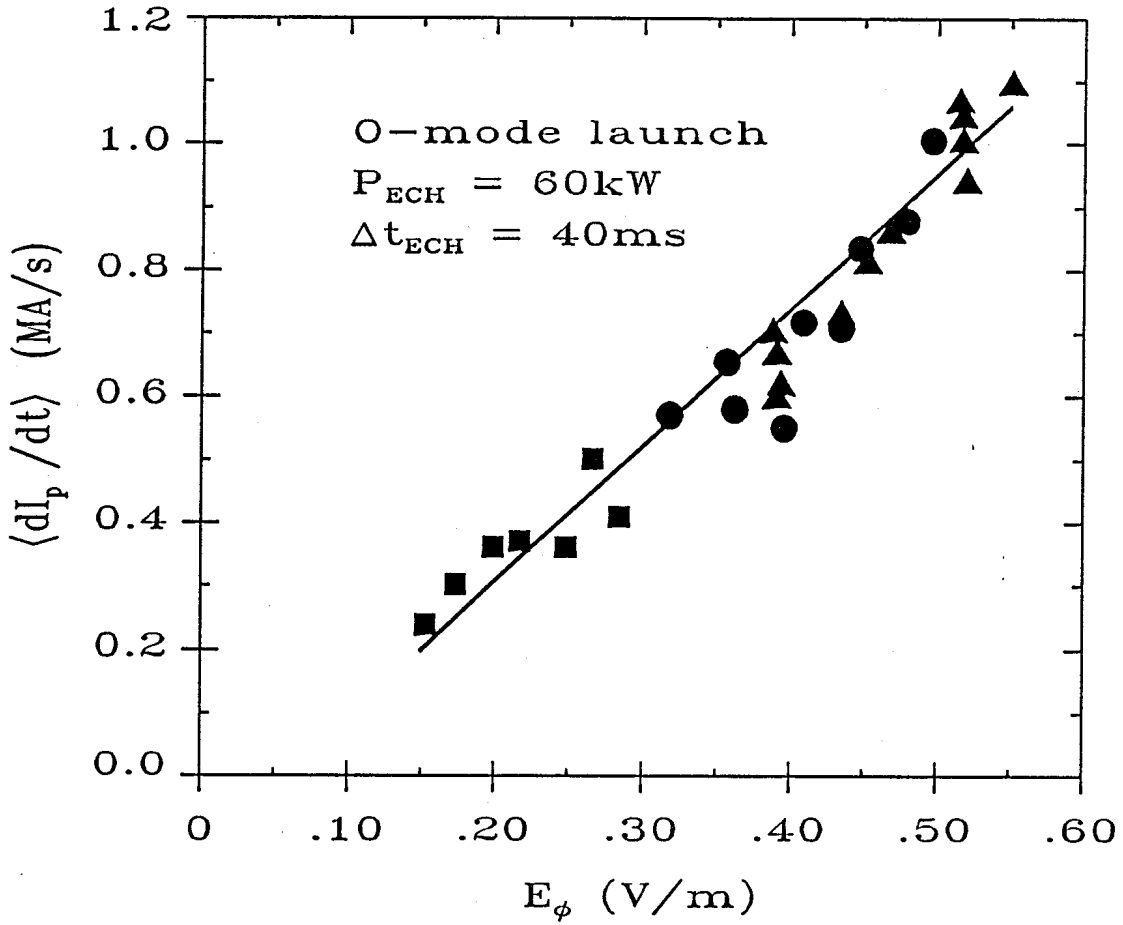
O-mode launch
P_{ECH} = 60kW
Δt_{ECH} = 40ms
$\langle dI_p/dt \rangle$ (MA/s)
E_ϕ (V/m)
0.0
0.2
0.4
0.6
0.8
1.0
1.2
0
.10
.20
.30
.40
.50
.60

Figure 18